Bioactive Materials 42 (2024) 345–365

Contents lists available at ScienceDirect

Bioactive Materials

journal homepage: www.keaipublishing.com/en/journals/bioactive-materials

# STING-activating dendritic cell-targeted nanovaccines that evoke potent antigen cross-presentation for cancer immunotherapy

Nguyen Thi Nguyen [a], Xuan Thien Le [a], Woo Tak Lee [a], Yong Taik Lim [b], Kyung Taek Oh [c], Eun Seong Lee [d], Han-Gon Choi [e], Yu Seok Youn [a,*]

[a] School of Pharmacy, Sungkyunkwan University, 2066 Seobu-ro, Jangan-gu, Suwon, Gyeonggi-do, 16419, Republic of Korea
[b] Department of Nano Engineering and School of Chemical Engineering, Sungkyunkwan University, 2066 Seobu-ro, Jangan-gu, Suwon, Gyeonggi-do, 16419, Republic of Korea
[c] College of Pharmacy, Chung-Ang University, 84 Heukseok-ro, Dongjak-gu, Seoul, 06974, Republic of Korea
[d] Department of Biotechnology and Department of Biomedical-Chemical Engineering, The Catholic University of Korea, 43 Jibong-ro, Bucheon-si, Gyeonggi-do, 14662, Republic of Korea
[e] College of Pharmacy, Hanyang University, 55 Hanyangdaehak-ro, Sangnok-gu, Ansan, 15588, Republic of Korea

ARTICLE INFO

*Keywords:*
DC-based nanovaccines
Artificial antigen-presenting cells
Type 1 conventional dendritic cells
STING pathway activation
Antigen cross-presentation

ABSTRACT

Recently, nanovaccine-based immunotherapy has been robustly investigated due to its potential in governing the immune response and generating long-term protective immunity. However, the presentation of a tumor peptide-major histocompatibility complex to T lymphocytes is still a challenge that needs to be addressed for eliciting potent antitumor immunity. Type 1 conventional dendritic cell (cDC1) subset is of particular interest due to its pivotal contribution in the cross-presentation of exogenous antigens to $CD8^+$ T cells. Here, the DC-derived nanovaccine (denoted as Si9GM) selectively targets cDC1s with marginal loss of premature antigen release for effective stimulator of interferon genes (STING)-mediated antigen cross-presentation. Bone marrow dendritic cell (BMDC)-derived membranes, conjugated to cDC1-specific antibody (αCLEC9A) and binding to tumor peptide ($OVA_{257-264}$), are coated onto dendrimer-like polyethylenimine (PEI)-grafted silica nanoparticles. Distinct molecular weight-cargos (αCLEC9A-$OVA_{257-264}$ conjugates and 2′3′-cGAMP STING agonists) are loaded in hierarchical center-radial pores that enables lysosome escape for potent antigen-cross presentation and activates interferon type I, respectively. Impressively, Si9GM vaccination leads to the upregulation of cytotoxic T cells, a reduction in tumor regulatory T cells (Tregs), M1/M2 macrophage polarization, and immune response that synergizes with αPD-1 immune checkpoint blockade. This nanovaccine fulfills a dual role for both direct T cell activation as an artificial antigen-presenting cell and DC subset maturation, indicating its utility in clinical therapy and precision medicine.

## 1. Introduction

Immune surveillance is a monitoring process by which the immune system recognizes and eliminates danger signals. When facing evasion by cancer cells, the immune system loses its ability for tumor eradication and function repair. Thus, cancer immunotherapy with recent advances in chimeric antigen receptor (CAR) T cell-therapy [1,2], cancer vaccination [3,4], and immune checkpoint blockade (ICB) [5–7] is considered a cornerstone in cancer treatment. Nanotechnology related to cell membrane-coated nanoparticles (NPs) has the potential to offer an extreme breakthrough in anticancer therapy [8], wherein biomimetic cell membranes expressing immune cell host-derived proteins with preserved function on the outer surface to enable prolonged nanoparticle blood circulation [9], leading to remarkable potential in recognizing antigens for selective targeting [10], gradual release of cargo [11], and enhanced biocompatibility in vivo [12,13]. Dendritic cells (DCs) are overwhelmingly important for innate immunity among various immune cells involved in antigen presentation [14]. DC membranes primarily express major histocompatibility complexes (MHCs) as the key membrane proteins responsible for the communication between DCs and other immune cells like T cells, natural killer cells (NK cells), and B cells [15–17]. Rather, DC membrane-coated NPs play as artificial

Peer review under responsibility of KeAi Communications Co., Ltd.
* Corresponding author.
*E-mail address:* ysyoun@skku.edu (Y.S. Youn).

https://doi.org/10.1016/j.bioactmat.2024.09.002
Received 8 May 2024; Received in revised form 16 August 2024; Accepted 1 September 2024

antigen-presenting cells (APCs) in the presence of tumor antigens, facilitating migration to lymph nodes (LNs) for T cell interaction, promoting potent anticancer immune responses [4,18–21].

Recently, the stimulator of interferon genes (STING) has been applied in preclinical anticancer therapy that is attributed to the good detection of pathogen utilizing STING as a danger sensor. However, the clinical data showed a limited efficacy in patients due to the fast clearance, poor membrane permeability, hydrophilic nature, and small molecular size of the free STING agonist [22,23]. Nanoparticle-based vaccines or nanovaccines (NVs) emerged as a promising strategy in cancer immunotherapy, with advanced focus on the co-delivery of antigens and adjuvants to address these challenges. Through STING pathway activation, type I interferon production drives multifaceted immune function in activating DC maturation and enhancing cross-presentation of tumor antigens for T cell-mediated immunity [24–28]. Given that STING is widely presented in various immune cells and cancer cells, selective STING activation in target cells plays a pivotal role in cancer immunotherapy. For example, activating STING pathway in T cells could both hamper T cell proliferation and cause apoptosis to T cells [29]. Besides that, STING activation in cancer cells enables $CD8^+$ T cell response but does not directly support antitumor efficacy in many cancer types [30–32]. Despite the huge expression of STING protein in DCs, the investigation on selective DC activation following STING pathway activation is limited. Therefore, the selective stimulation of a STING agonist to a specific immune cell like DC should be considered. Recently, type 1 conventional dendritic cells (cDC1), a dendritic cell subpopulation, have been identified as promoting innate and adaptive immune response [33]. cDC1s adept exceptional abilities in presenting

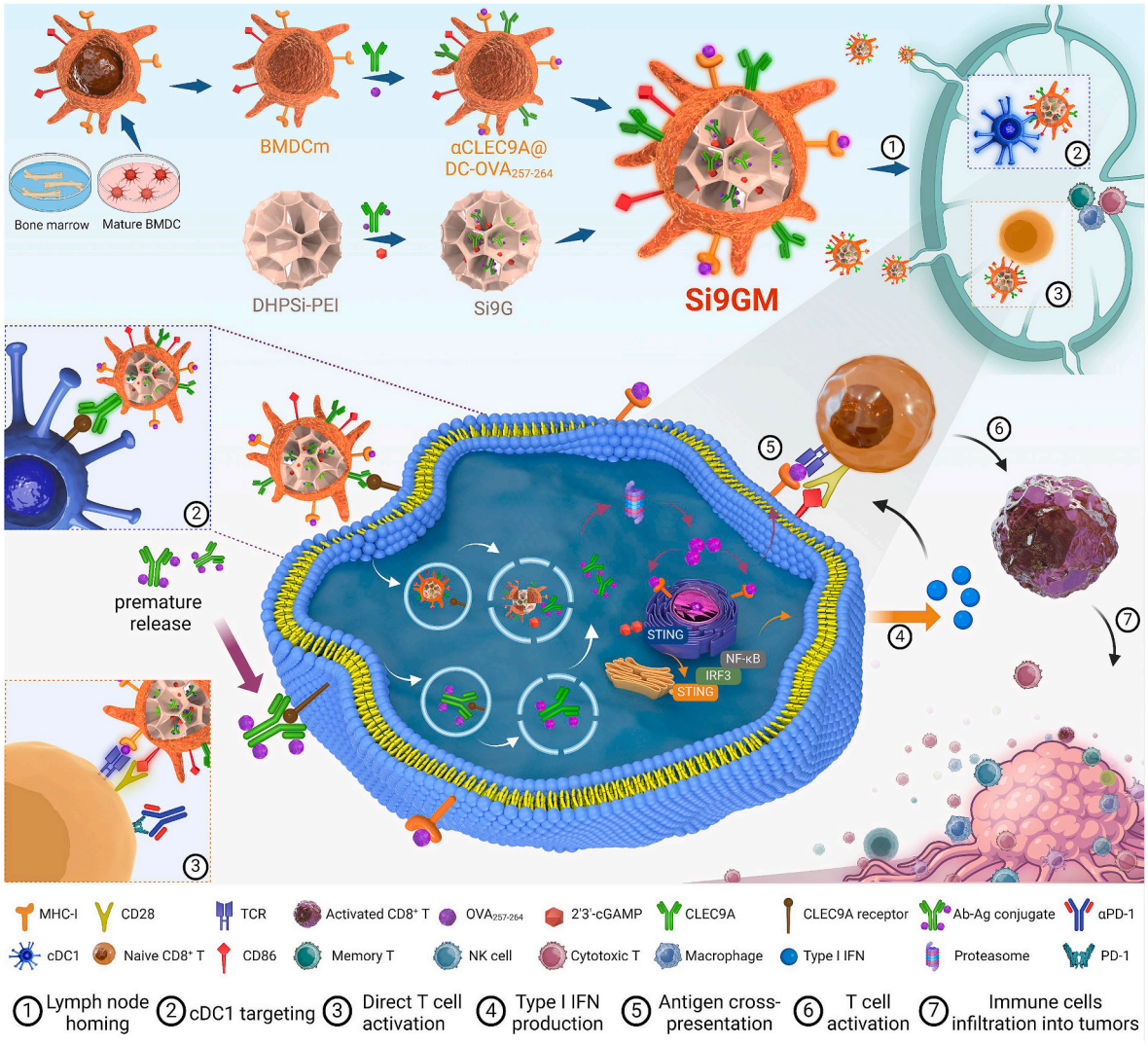


**Scheme 1.** Fabrication and therapeutic mechanisms of Si9GM. Fabrication steps: bone mesenchymal stem cells were isolated from femurs and tibias of C57BL/6 mice, and then stimulated to obtain immature bone marrow-derived dendritic cells (BMDCs). After activation, mature BMDCs were collected, followed by extraction to obtain BMDC membranes (BMDCm). Next, antigen peptides ($OVA_{257-264}$) were loaded onto BMDCm by binding to major histocompatibility complex class I (MHC I) molecules using a pH-dependent method. The obtained membranes (DC-$OVA_{257-264}$) were then conjugated with αCLEC9A using sulfo-SMCC/Traut's reagent linkers to produce BMDC membranes containing $OVA_{257-264}$ and αCLEC9A antibodies, denoted as αCLEC9A@DC-$OVA_{257-264}$. In addition, dendrimer-like hierarchical large pore silica nanoparticles were synthesized using the quasi-emulsion nanodroplet method. These nanoparticles were then loaded with αCLEC9A-$OVA_{257-264}$ conjugates and 2′3′-cGAMP STING agonist, denoted as Si9G. Finally, Si9G NPs were coated with αCLEC9A@DC-$OVA_{257-264}$ to generate Si9GM nanovaccines. Therapeutic mechanisms of Si9GM: Si9GM nanovaccines were effectively delivered to LNs, where Si9GM acts both as an artificial antigen-presenting cell and as a DC activator for directly presenting antigen on $CD8^+$ T cells and DC maturation, respectively. αCLEC9A on the Si9GM surface selectively target type 1 conventional DCs (cDC1s), where the released αCLEC9A-$OVA_{257-264}$ conjugates and 2′3′-cGAMP STING agonist play critical roles in antigen cross-presentation and STING pathway activation, respectively. Furthermore, nanovaccine Si9GM in combination with immune checkpoint blockade (αPD-1) promoted potent antitumor immunity for effective cancer immunotherapy and metastasis inhibition.

both endogenous and exogenous antigens to T cells, promoting T cell activation and proliferation for empowering anticancer therapy. This distinctive role of cDC1s holds great potential, particularly in nanovaccine-based therapies, wherein cDC1s capture antigens originating from nanovaccines and present them to $CD8^+$ T cells after homing to tumor-draining lymph nodes (tdLNs) or infiltrating to the tumor microenvironment (TME). Therefore, selective antigen cross-presentation in cDC1s promises great attention in cancer immunotherapy.

CLEC9A is a C-type lectin endocytosis receptor expressed on cDC1

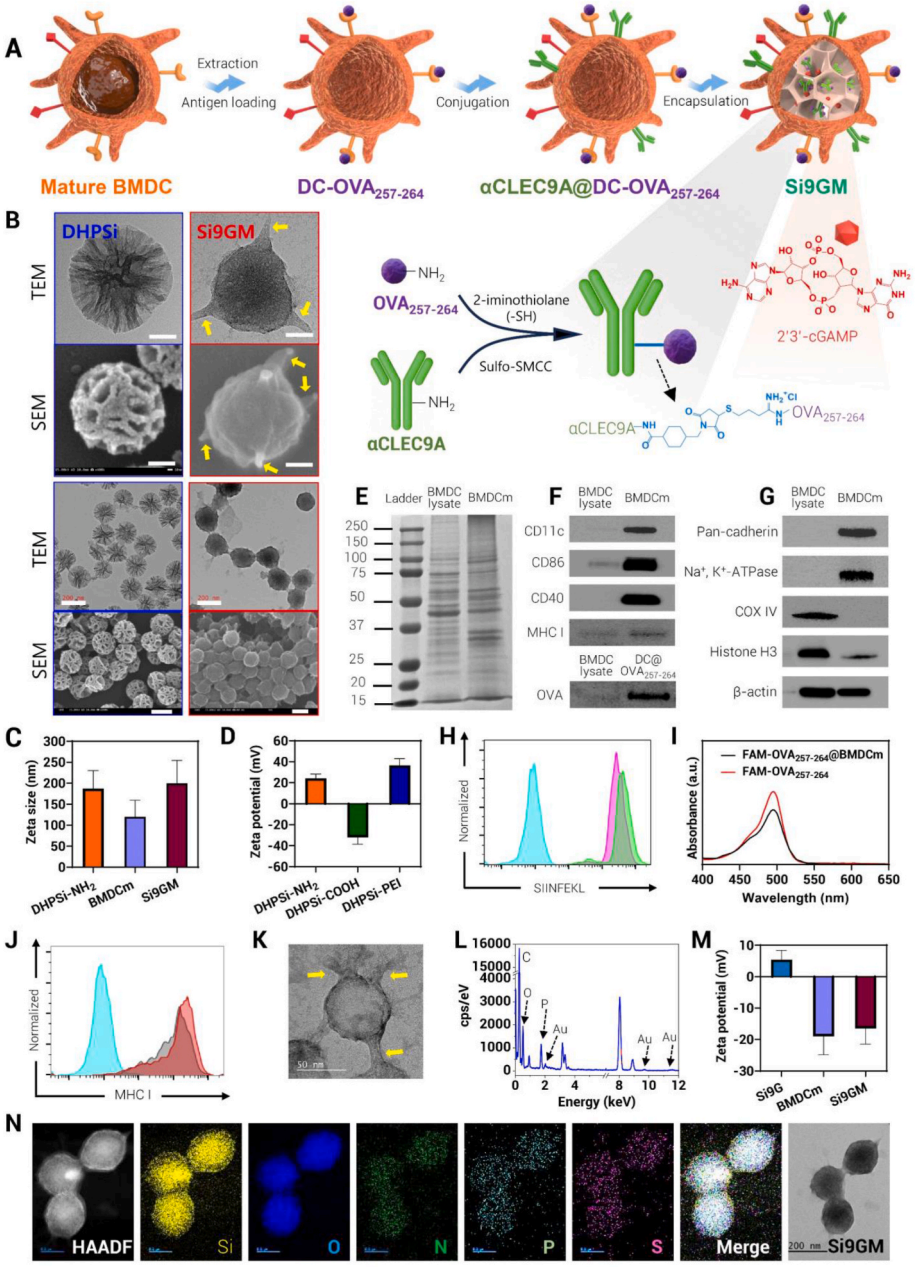


**Fig. 1.** Preparation and characterization of Si9GM. (A) Schematic representation of Si9GM nanovaccine formulation involving coating modified BMDC membranes on center-radial large pore silica NPs, loading αCLEC9A-$OVA_{257-264}$ conjugates and 2′3′-cGAMP STING agonists. (B) TEM and SEM images of DHPSi NPs and Si9GM (white scale bars: 50 nm), yellow arrows: projections of BMDC membranes. (C) Hydrodynamic size of DHPSi-$NH_2$, BMDCm, and Si9GM. (D) Zeta potential of DHPSi-$NH_2$, DHPSi-COOH, and DHPSi-PEI. (E) SDS-PAGE of BMDC lysates and BMDC membranes extracted from BMDCs post LPS-induced activation (1 μg $mL^{-1}$) for 24 h (denoted as BMDCm). (F) Western blot analysis of surface proteins of cell lysates and BMDCm and antigen peptide loaded BMDCm (denoted as DC-$OVA_{257-264}$). (G) Western blot assays of membrane-derived biomarkers and intracellular proteins in the BMDC lysate and BMDCm-extracted protein. (H) Flow cytometric analysis of the presence of antigen peptides $OVA_{257-264}$ on BMDC membranes after loading antigen fragments on MHC I molecules by pH-dependent mechanism, blue: unstained BMDCm, pink: DC-$OVA_{257-264}$ ($OVA_{257-264}$: 50 μg per 1 mg of BMDCm), green: DC-$OVA_{257-264}$ ($OVA_{257-264}$: 100 μg per 1 mg of BMDCm). (I) Analysis of the loading of antigen peptides $OVA_{257-264}$ on BMDCm by UV–vis measurement. (J) Analysis of the presence of MHC I on BMDCm by flow cytometry, blue: unstained BMDCm, grey: 1-month stored BMDCm, red: 2-month stored BMDCm. (K) TEM image DC-$OVA_{257-264}$ (yellow arrows: dendrite structure of DC). (L) Energy dispersive spectroscopy (EDS) analysis of Au-labeled antibody-conjugated αCLEC9A@ DC-$OVA_{257-264}$, showing the presence of Au atoms represented for the successful conjugation of αCLEC9A on the surface of DC-$OVA_{257-264}$. Scale bar: 100 nm. (M) Zeta potential of DHPSi NPs loading αCLEC9A-$OVA_{257-264}$ conjugates and 2′3′-cGAMP agonists (denoted as Si9G), BMDCm, and DC-$OVA_{257-264}$ coated Si9G nanovaccine (denoted as Si9GM). (N) EDS mapping analysis of elements (Si, O, N, P, S) in Si9GM nanovaccine.

cells, responsible for the endocytic uptake of antigens and initiating subsequent antigen cross-presentation on $CD8^+$ T cells [34]. The endocytosed antigen-CLEC9A complex is non-localized with the lysosomal compartment, facilitating the effective retrieval of antigens for cross-presentation and enhancing cancer immunotherapy effectiveness [35,36]. Furthermore, CLEC9A-targeted antigens have been shown to elicit more robust immune responses compared to antigens targeted to another receptor on cDC1s (DEC205) [37]. Therefore, the selective activation of STING in cDC1s by CLEC9A-targeted nanovaccines holds tremendous potential for advancing research in cancer immunotherapy.

Herein, we report a bone marrow DC-based nanovaccine (denoted as Si9GM) formulated from antigen peptide-expressed bone marrow-derived dendritic cell (BMDC) membrane engulfing center-radial large pore silica nanoparticle for the effective transport of αCLEC9A-antigen conjugate and STING agonist (2′3′-cGAMP) (Scheme 1, and Fig. 1A). BMDCs were isolated and stimulated in vitro, following engulfed $CD8^+$ T cell-specific antigen fragments ($OVA_{257-264}$) to obtain an antigen peptide-presented determinant (denoted as M). CLEC9A antibody conjugated $OVA_{257-264}$ fragments and 2′3′-cGAMP were loaded in the centered-radial large pores of dendritic silica NPs (denoted as Si9G) for their co-delivery and protection from enzymatic degradation. The nanovaccine served a dual role as an artificial APC for T cell activation and an activator for DC maturation, especially in indispensable cDC1 subset. Notably, the released antigen-CLEC9A conjugate and 2′3′-cGAMP played a critical role in cDC1 with cross antigen presentation for the former and type I IFN production for the latter. The LN homing ability of the nanovaccines identified by the extensive accumulation of NVs (rather than those by free STING agonist injection) prompted us to study its competency in generating antitumor efficacy. We also proved that the combination with αPD-1 blockade could induce a robust tumor growth inhibition and metastasis prevention. This promising therapeutic efficacy could provide the multifaceted functions of DC-based nanovaccines for personalized cancer immunotherapy and precision medicine.

## 2. Results and discussion

### 2.1. Formulation of BMDC-based nanovaccines Si9GM

To carry therapeutic antibodies and other high molecular weight molecules around 150 kDa, variable delivery systems like liposomes [38], microparticles [39], PLGA [40] have been reported. However, using inorganic NPs to deliver high molecular weight (M.W.) molecules is still challenging. In this work, we leveraged new dendrimer-like silica NPs with hierarchical pores (DHPSi NPs) in which special center-radial large pore size formed gradually from the particle center to its outer surface [41]. This distinctive morphology endows NPs with the super-high loading capacity of large molecules and tailors the cargo release. The combination of pores with multi-scale structures supports the co-loading of encapsulated molecules with different sizes through porous matrices. DHPSi-$NH_2$ NPs were synthesized using the ethyl ether emulsion approach (Fig. S1). After purification, DHPSi-$NH_2$ NPs were formulated with high homogeneity, large center-radial dendritic pores and small size (<200 nm) (Fig. 1B). The size of NPs and surface zeta potential (zeta P) were determined utilizing a Zetasizer Nano ZS from the Malvern instrument (Fig. 1C and D). For effective loading of a highly hydrophilic small molecule such as 2′3′-cGAMP (denoted as G), we modified the amine functional groups to carboxylic groups, followed by conjugation with low M.W. (M.W. = 0.8 kDa) branched polyethylenimine (PEI) to generate DHPSi-PEI NPs. This facile method of introducing branched low-molecular-weight positively charged polymer provided nanoparticles with excellent biocompatibility, minimal toxicity, and high colloidal stability. Notably, it favored the encapsulation efficiency (EE) of anionic 2′3′-cGAMP into DHPSi-PEI NPs through electrostatic binding, achieving a 53 % of EE compared to that of DHPSi-$NH_2$ (9 %) (Fig. S2). The successful modification of surface functional groups was evaluated by the measurement of zeta P, in which zeta P values of DHPSi-$NH_2$, DHPSi-COOH and DHPSi-PEI were +24.2 ± 4.10 mV, −32.1 ± 6.46 mV, and +36.5 ± 6.47 mV, respectively (Fig. 1D, Fig. S3). Furthermore, characterization by Fourier-transform infrared spectroscopy (FTIR) reaffirmed the functional groups of the surface-modified DHPSi NPs. The presence of N–H bending vibration and C–N stretching vibration, respectively at 1561 $cm^{-1}$ and 1402 $cm^{-1}$, highlighted the transformation from –$NH_2$ groups into –COOH groups. The enhancing bands at 1464 $cm^{-1}$, 2856 $cm^{-1}$, and 2954 $cm^{-1}$ indicated the PEI conjugation (Fig. S4).

DC-derived membranes were prepared by stimulation of primary cells from mouse bone marrow. On day 8 post-stimulation, non-adherent BMDCs were collected and characterized by flow cytometric analysis to characterize the population of BMDCs ($CD11c^+$ $F4/80^-$). We obtained more than 84 % $CD11c^+$ $F4/80^-$ DCs, confirming the high purity of BMDCs (Fig. S5A and Fig. S6A). Mature BMDCs were obtained through lipopolysaccharide (LPS) activation, and mature DC biomarkers were characterized by flow cytometry (Fig. S5B and C, Fig. S6B and C). After extraction, the purity and preservation of immune biomarkers in BMDC membranes (referred to as BMDCm) were verified. Specifically, sodium dodecyl sulfate-polyacrylamide gel electrophoresis (SDS-PAGE) was carried out on both BMDC lysates and membranes to confirm protein integrity. As shown in Fig. 1E, comparable bands were detected in both BMDC lysates and BMDCm, suggesting that the integrity of the membranes was effectively maintained throughout the extraction and storage processes. BMDCs were activated by LPS to maximize the expression of membrane-located co-stimulatory molecules [42]. For verification, the retention of critical DC membrane proteins (including CD11c, CD86, and CD40) on the BMDC surface was further confirmed by Coomassie blue staining. As presented in Fig. 1F, protein bands of CD11c, CD86, and CD40 were only found in BMDCm but not in BMDC lysates, confirming the purity of extracted BMDCm containing well-retained immune biomarkers. Furthermore, the proteins extracted from the obtained BMDCs lysates and membranes were analyzed with Western blot assays for a series of protein markers. The data verified the successful extraction of BMDCm whereby transmembrane glycoprotein (Pan Cadherins) and essential plasma membrane enzyme ($Na^+/K^+$-ATPase) were well-preserved after extraction and storage. The study also examined the presence of representative intracellular proteins, such as Cytochrome C oxidase subunit 4 isoform 1 (COX IV), Histone H3, and β-actin, which are found in the mitochondria, nucleus, and cytosol, respectively. The lack of Histone H3 and COX IV in BMDCm confirmed the effective separation between membranes and lysates, indicating minimal risk of carcinogenesis (Fig. 1G) [33].

To enhance the T cell-stimulatory capacity of DC-based nanovaccines, BMDCm needs to present antigen-expressed MHC I complexes. According to previous research, peptide fragments robustly bind to MHC I molecules at acidic pH (5.0–5.5) compared to neutral pH [43]. In addition, the peptide-MHC class I complex was stabilized at neutral pH (Fig. S7) [18]. Therefore, $OVA_{257-264}$ peptides were loaded onto MHC class I molecules of BMDCm by a pH-dependent exchange reaction to generate $OVA_{257-264}$-loaded BMDCm (denoted as DC-$OVA_{257-264}$), and then DC-$OVA_{257-264}$ were conjugated with αCLEC9A using thiol-maleimide chemistry (Fig. S8). For verification of the successful loading of $OVA_{257-264}$ antigen fragments on BMDCm, 5-Carboxyfluorescein-conjugated $OVA_{257-264}$ (FAM-$OVA_{257-264}$) was used as a replacement for $OVA_{257-264}$, and the expression of FAM-$OVA_{257-264}$ was characterized by flow cytometry and the absorbance measurement of naïve BMDCm and DC-$OVA_{257-264}$ at a wavelength of 495 nm (Fig. 1H and I). The data showed an increase in absorbance of DC-$OVA_{257-264}$ compared to BMDCm, confirming the loading of $OVA_{257-264}$ on BMDCm by a pH-dependent reaction (Fig. 1I). Furthermore, the presence of antigen peptides on DC-$OVA_{257-264}$ was confirmed by Western blot assay (Fig. 1F). In addition to antigen fragments, the expression of MHC I molecules required for antigen presentation was also analyzed by flow cytometry. Likewise, the increased fluorescent intensity of BMDCm stained by (Alexa fluor 647) AF647-MHC I antibody compared to control

sample (unstained BMDCm) after long-term storage emphasized the availability of MHC I molecules for antigen presentation on BMDCm and the well-retained surface biomarkers (Fig. 1J). For verification of the successful conjugation of αCLEC9A, DC-OVA$_{257-264}$ nanovesicles were incubated with gold-labeled IgG antibodies and then characterized by TEM-supplemented elemental mapping (EDS) (Fig. 1K and L). As shown in Fig. 1L, the peaks of Au elements confirmed the presence of conjugated αCLEC9A on DC-OVA$_{257-264}$ nanovesicles.

The coating of BMDCm onto DHPSi NPs was characterized by TEM and SEM images, verifying the well-coated NPs and the dendritic structure of BMDC membranes (yellow arrows) (Fig. 1B). The colloidal stability of Si9GM was evaluated in Fig. S9A. Furthermore, the release profile of 2′3′-cGAMP in different pH was investigated by high-performance liquid chromatography (HPLC) (Fig. S9B). Impressively, the presence of DC-derived projections (yellow arrows) highlighted the unique feature of BMDCm-coated NPs, confirming the mild membrane extraction process for maintaining the surface biomarkers for immune responses. The zeta potential measurement further confirmed the well-coated modified BMDCm onto DHPSi NPs (Fig. 1M). The EDS mapping data showed the presence of various elements such as Si, O, N, P, and S in Si9GM NPs, reaffirming the successful coating of BMDCm onto Si9G NPs. Notably, the element mapping of P and S represents the BMDC membranes and CLEC9A antibodies, respectively (Fig. 1N).

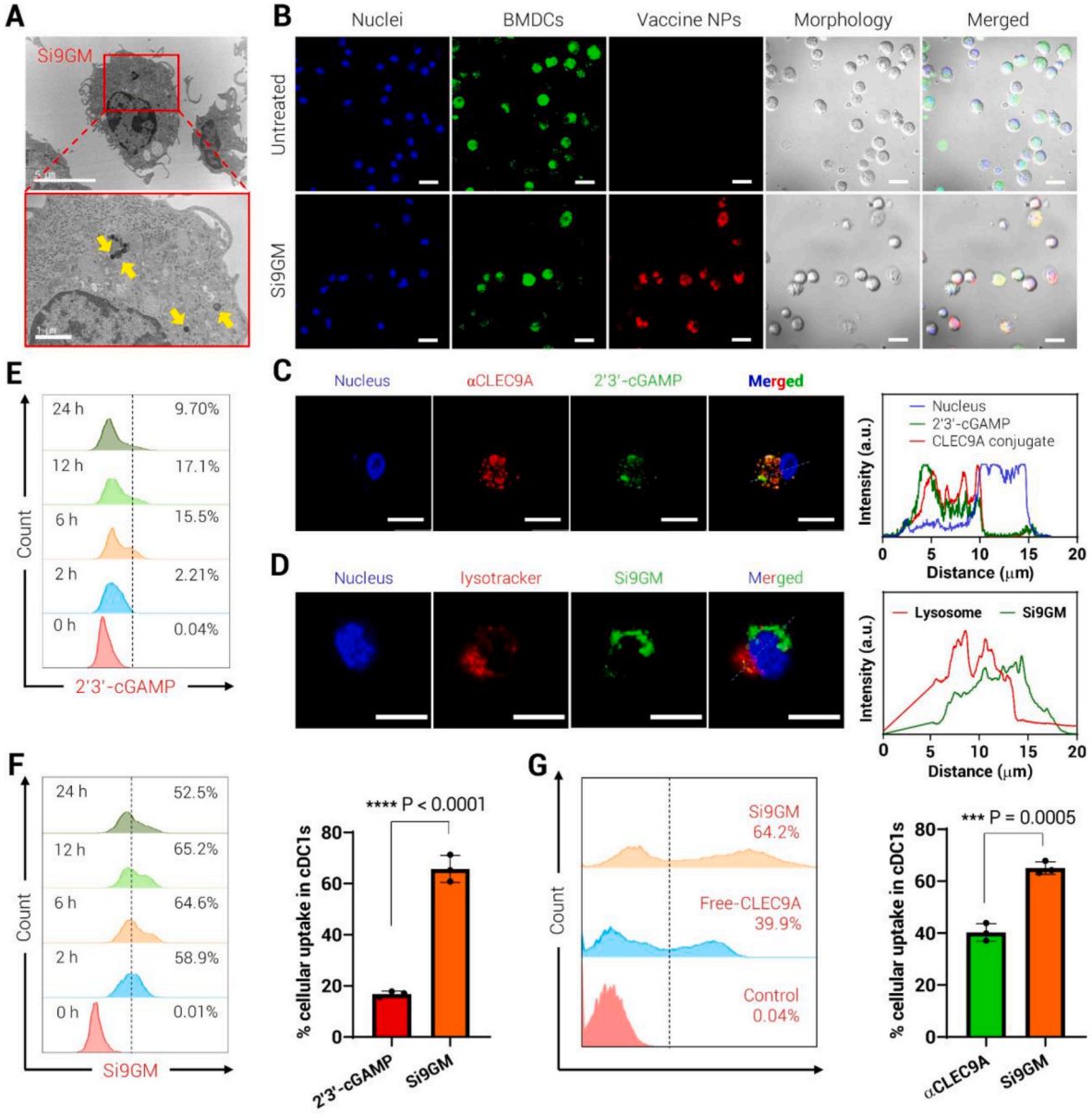


**Fig. 2.** DC internalization of Si9GM. (A) Bio-TEM images of Si9GM internalized into BMDCs, the yellow arrows point out the uptake of Si9GM, scale bars: 5 μm and 1 μm. (B) Cellular uptake of Si9GM into BMDCs was analyzed by CLSM, green: neuro-DiO; red: DiI, blue: Hoechst 33342, scale bar: 20 μm. (C) Determination of αCLEC9A-OVA$_{257-264}$ and 2′3′-cGAMP delivered by Si9GM into cDC1s by CLSM, blue: nucleus; red: AF647-labeled CLEC9A conjugate; green: cFAET-labeled 2′3′cGAMP, scale bar: 10 μm. (D) Investigation of lysosome escape ability of Si9GM in cDC1s, blue: nucleus; red: lysotracker Red; green: Si9GM loading cFAET-labeled 2′3′-cGAMP, scale bar: 10 μm. (E) Analysis of free 2′3′-cGAMP uptake into cDC1s by flow cytometry. (F) Analysis of 2′3′-cGAMP delivered by Si9GM into cDC1s by flow cytometry. (G) Comparison of the uptake of free αCLEC9A conjugates and αCLEC9A-OVA$_{257-264}$ conjugate delivered by Si9GM into cDC1s by flow cytometry. Column graphs showed data presented as the mean ± standard deviation, with statistical significance calculated via two-tailed Student's t-test (F,G). P > 0.05 stands for not significant (ns), *P < 0.05; **P < 0.01; ***P < 0.001; ****P < 0.0001.

### 2.2. Si9GM NPs enhanced cellular uptake of 2′3′-cGAMP -in DCs

For verification of cellular uptake of BMDC-derived nanovaccines in DCs, we utilized bio-TEM measurement on BMDCs. As shown in Fig. 2A, we observed that Si9GMs (yellow arrows) internalized into BMDCs after 8 h of incubation. The uptake of Si9GM in BMDCs was further confirmed by confocal laser scanning microscopy (CLSM), in which BMDCs and Si9GMs were stained by neuro-DiO (green) and DiI (red), respectively. The presence of overlapping areas (yellow color) in the merged image confirmed the internalization of NVs into BMDCs (Fig. 2B). Similar results were obtained in the DC2.4 cell line (Fig. S10). Importantly, the targeting capacity of Si9GM to cDC1 cells was studied by CLEC9A receptor blocking assay (Fig. S11A). As shown in Fig. S11B, the uptake of Si9GM in cDC1s (54.5 ± 2.15 %) is higher than in CLEC9A-blocking cDC1s (44.1 ± 0.36 %). Meanwhile, the uptake of SiGM nanovaccines (without CLEC9A-targeting BMDC membrane coating) in non-CLEC9A blocking cDC1s and CELC9A blocking cDC1s is similar (44.0 ± 1.87 % and 42.1 ± 1.63 %, respectively). Therefore, it is apparent that Si9GM presented better uptake in cDC1s compared to that of SiGM. Furthermore, we investigated the delivery of αCLEC9A-$OVA_{257-264}$ and 2′3′-cGAMP by DHPSi-PEI NPs into cDC1s, BMDCs by CLSM (Fig. 2C and Figs. S12, S13). As illustrated in Fig. 2C, the red fluorescence and green fluorescence represented AF647-labeled αCLEC9A-$OVA_{257-264}$ conjugate and cyclic (8- (2- [fluoresceinyl]aminoethylthio)-labeled 2′3′-cGAMP (denoted as cFAET-labeled 2′3′-cGAMP), respectively, verifying their co-loading into DHPSi-PEI NPs. The alone loading of STING agonist, and αCLEC9A-$OVA_{257-264}$ in DHPSi-PEI NPs was further investigated in BMDCs by CLSM (Fig. S14). The data represented that the alone loading of small molecules 2′3′-cGAMP was efficient without the support of large M.W. αCLEC9A-$OVA_{257-264}$ conjugate, reaffirming the potential role of branched PEI to bind anionic small molecules.

To achieve cytosolic delivery of αCLEC9A-$OVA_{257-264}$ and STING agonist, Si9GM NPs must escape lysosomal compartments once they internalized into the endo/lysosomes [44]. The efficient release of Si9GM NPs from a lysosomal compartment was evaluated by the negligible presence of overlapping fluorescence (yellow area), favoring the delivery of cargo to present antigen peptides on MHC I molecules and activate STING pathway in cDC1s (Fig. 2D and Fig. S15). In contrast, free STING agonist 2′3′-cGAMP showed a low ability to escape lysosome (Fig. S16), verifying the potential of Si9GM nanovaccines to elicit antigen cross-presentation on MHC I molecules followed with stimulation of T cells and NK cells. In more detail, the lysosomal escape of Si9GM in cDC1s by time was also investigated (Fig. S17).

STING agonist, albeit to be highlighted as a potential small molecule in cancer immunity due to the ability to promote DCs maturation, is limited applied in cancer immunotherapy [45,46]. The highly negatively-charged characteristic of STING agonists prevents them from being effectively taken up by DCs [47], and it triggers a less potent stimulation of the immune system. To further verify the cellular uptake of 2′3′-cGAMP in cDC1s, in vitro cDC1s were treated by cFAET-labeled 2′3′-cGAMP as free molecules and encapsulated form in NVs, and the effectiveness of cellular internalization was examed by flow cytometric analysis. Consistent with the outcomes observed in BMDCs, the uptake of free STING agonist (cFAET-labeled-2′3′cGAMP) in cDC1s was negligible and marginally increased over time, reaching a maximum value of 16.8 ± 1.12 % after 12 h of incubation (Fig. 2E). In contrast, Si9GM NPs delivered 2′3′-cGAMP more effectively, with 65.8 ± 5.27 % of cDC1s positive for cFAET-2′3′cGAMP (Fig. 2F). Taken together, these results indicate the potential of the Si9GM nanovaccines as a delivery system for free STING agonists, overcoming certain limitations in cancer immunotherapy. Next, we investigated the role of Si9GM in enhancing αCLEC9A-$OVA_{257-264}$ conjugates uptake in cDC1s. Similarly, we found that the center-radial large pore structure of DHPSi NPs effectively delivered high M.W. conjugate (65.1 ± 2.42 %) to cDC1s compared to free CLEC9A-$OVA_{257-264}$ conjugates (40.3 ± 3.42 %) (Fig. 2G).

### 2.3. Si9GMs play a key role as artificial antigen-presenting cells for direct CD8 T cell activation

For verification of the role of Si9GM NVs as artificial APCs, isolated $CD8^+$ T cells from mice spleens were treated with Si9GM NVs. We observed an interaction between Si9GMs (red fluorescence) on the T cell surface (green fluorescence), confirming that the $OVA_{257-264}$-MHC I complexes onto BMDC membranes of Si9GM nanovaccines facilitated interaction with $CD8^+$ T cells, thus demonstrating the role of Si9GM NPs as artificial APCs (Fig. 3A). Meanwhile, $CD8^+$ T cells treated by NVs in the absence of the loading of $OVA_{257-264}$ fragments on BMDC membranes showed minimal interaction between NPs and T cells, with the majority of Si9GMs localized in the cytosol (Fig. S18). It is reported that the STING agonist induces apoptosis in a manner specific to T cells, but not in BMDCs or bone marrow-derived macrophages (BMDMs) [48]. Therefore, the loading of $OVA_{257-264}$ antigen fragments onto mature BMDC membranes not only activates T cells but also prevents the uptake causing apoptosis in $CD8^+$ T cells. For verification of Si9GM as an artificial APC, we investigated the capacity of Si9GM in $CD8^+$ T cell activation by direct incubation between nanovaccines and $CD8^+$ T cells isolated from OT-I mice. After 20 h of incubation, the population of activated $CD8^+$ T cells ($CD8^+$ $CD69^+$) reached approximately 49.9 ± 4.33 %, which is higher compared to $CD8^+$ T cells treated with $OVA_{257-264}$ loaded mature BMDC membranes (DC-OVA, 38.3 ± 4.41 %) and immature BMDC-derived Si9GM (Si9GimM, 25.9 ± 3.58 %) (Fig. 3B and C). As a result of T cell activation, it exhibited the highest proliferation of $CD8^+$ T cells when treated with Si9GM, consistent with the level of T cell activation (Fig. 3D and E). Given the most effective T cell activation induced by Si9GM, the cytotoxic effect of these $CD8^+$ T cells was investigated by incubating them with B16-OVA cancer cells for 20 h, and the killing efficiency was determined by flow cytometry (Fig. 3F and G). As demonstrated in Fig. 3F, the necrosis and apoptosis populations of B16-OVA cancer cells incubated with Si9GM-induced cytotoxic $CD8^+$ T cells increased up to 29.1 % and 38.4 %, respectively, which were higher than those of DC-OVA- and Si9GimM-treated $CD8^+$ T cell groups. The capacity of Si9GM for direct $CD8^+$ T cell activation, proliferation, and killing efficacy was evaluated in comparison with Dynabeads Mouse T-Activator CD3/CD28. Dynabeads showed higher efficacy compared to Si9GM, which could be attributed to the larger size of Dynabeads (4.5 μm) compared to that of Si9GM nanovaccines. Similarly, Si9GM showed better performance than DC-OVA due to the size-dependent T-cell activation [49]. Thanks to these findings, it can be concluded that Si9GM nanovccines play a pivotal role in $CD8^+$ T cell direct activation, proliferation, and cytotoxic T cell-caused killing efficacy of cancer cells, promising the potential of Si9GM in cancer immunotherapy.

### 2.4. Si9GMs stimulate STING pathway activation and augment DC maturation

Many studies have shown that 2′3′-cGAMP binds to STING dimers at the endoplasmic reticulum (ER) membrane, promoting the ER-to-Golgi translocation of STING [50]. This early-stage activation leads to STING oligomerization triggered by conformational changes, facilitating subsequent downstream signals [51]. As shown in Fig. 4A, STING assists in the recruitment of TANK-binding kinase 1 (TBK1), enhancing its autophosphorylation (p-TBK1), phosphorylation of STING and interferon regulatory factor 3 (IRF3). pTBK1 catalyzes IRF3 for dimerization, and those dimers translocate to the nucleus to induce gene expression of type I interferons (type I IFN) and other inflammatory genes [52]. In addition, STING activation leads to the phosphorylation of nuclear factor kappa B (NK-κB), promoting the transcription of genes encoding a series of proinflammatory cytokines [53]. To verify the STING pathway activation of Si9GM and free 2′3′-cGAMP, Western blot assays were carried out to evaluate the upregulation of type I IFN-induced proteins. As displayed in Fig. 4B, the phosphorylation levels of TBK1 (p-TBK1), STING (p-STING), (IRF3) p-IRF3, and (NK-κB) p-NK-κB were increased

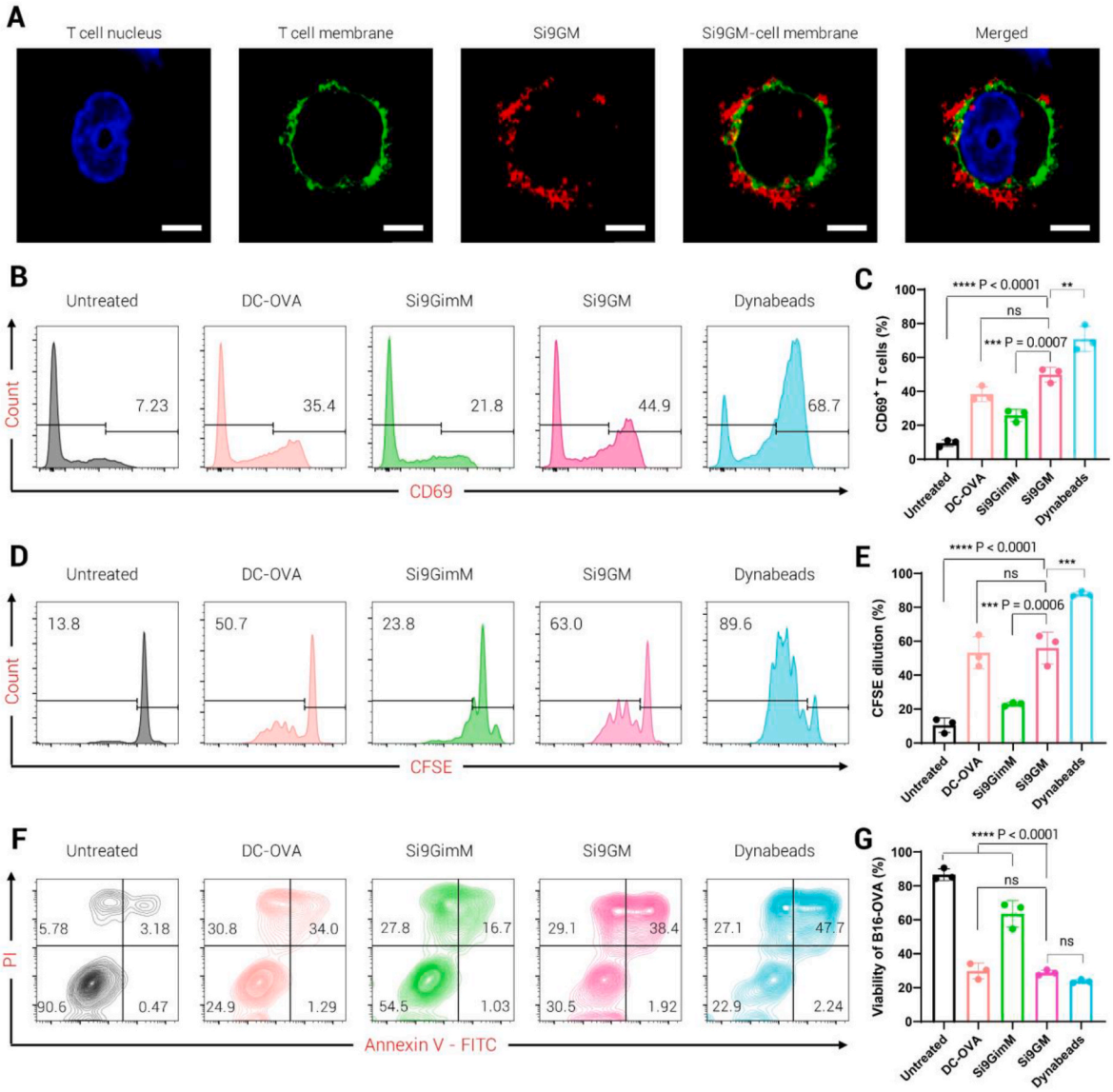


**Fig. 3.** (A) Evaluation of the role of Si9GM as an artificial antigen-presenting cell through the interaction with $CD8^+$ T cell, blue: Hoechst 33342, green: neuro-DiO, red: DiI, scale bar: 5 μm). (B, C) Representative flow cytometric plots and percentage of activated $CD8^+$ OT-I T cells after 20 h of various treatments. (D, E) Representative flow cytometric plots and percentage of proliferating $CD8^+$ OT-I T cells after 4 days of various treatments. (F, G) Representative flow cytometric plots and viability percentage of cytotoxic $CD8^+$ T cell-induced cancer cells after 20-h co-incubation. The data is presented as the mean ± standard deviation, with statistical significance determined using one-way ANOVA with Tukey's test (C, E, G) with Tukey's test (F). $P > 0.05$ stands for not significant (ns), *$P < 0.05$; **$P < 0.01$; ***$P < 0.001$; ****$P < 0.0001$.

after Si9GM incubation in comparison with free 2′3′-cGAMP that is attributed to the efficient delivery of STING agonist to BMDCs by Si9GM NVs over free STING agonists. Furthermore, the production of IFN-β in Si9GM-treated BMDCs was higher compared to that in 2′3′-cGAMP-treated BMDCs (Fig. 4C). The result suggested that Si9GM displayed a predominant role in augmenting STING signaling cascade and type-I IFN production, potentiating Si9GM for robust DC activation and immune response.

Given that STING activation promotes DC maturation, we carried out the in vitro BMDC activation upon the treatment of 2′3′-cGAMP and Si9GM. When exposed to inflammatory and pathogenic signals, immature DCs undergo maturation, exhibiting the upregulation of costimulatory molecules and MHC II molecules, which promotes the antigen presentation and upregulates the chemokine receptor CCR7 [54]. Therefore, the role of Si9GM in promoting DC maturation, antigen cross-presentation, and LN homing was studied with BMDCs in vitro and compared to that of free 2′3′-cGAMP. After 24 h of incubation, co-stimulatory molecules CD40, CD80, CD86, and MHC II were stained and identified by flow cytometry. As illustrated in Fig. 4D and Fig. S19, the increased population of $CD40^+$ $CD11c^+$, $CD86^+$ $CD11c^+$, and MHC $II^+$ $CD11c^+$ were expressed in BMDCs treated with Si9GM compared to those treated with free 2′3′-cGAMP. The difference was attributed to the active targeting of free STING agonists to DCs through BMDC membrane coating. Next, we investigated the ability of DCs for cross-presentation of the MHC-I-restricted OVA epitope SIINFEKL for $CD8^+$ T cell activation. The percentage of $SIINFEKL^+$ $CD11c^+$ greatly increased in the Si9GM-treated BMDCs (22.2 ± 0.96 %) compared to those treated with 2′3′-cGAMP (15.6 ± 1.39 %), indicating that presentation of antigen peptides by STING stimulation-induced cross-presentation was more effective in Si9GM-treated BMDCs.

CCR7, a type of C-C chemokine receptor, triggers the homing of CCR7-expressed dendritic cells to the lymph nodes [55]. Since DCs need to be recruited into LNs where T cells are abundantly localized to induce antigen-specific T cells, the population of $CD11c^+$ $CCR7^+$ DCs was

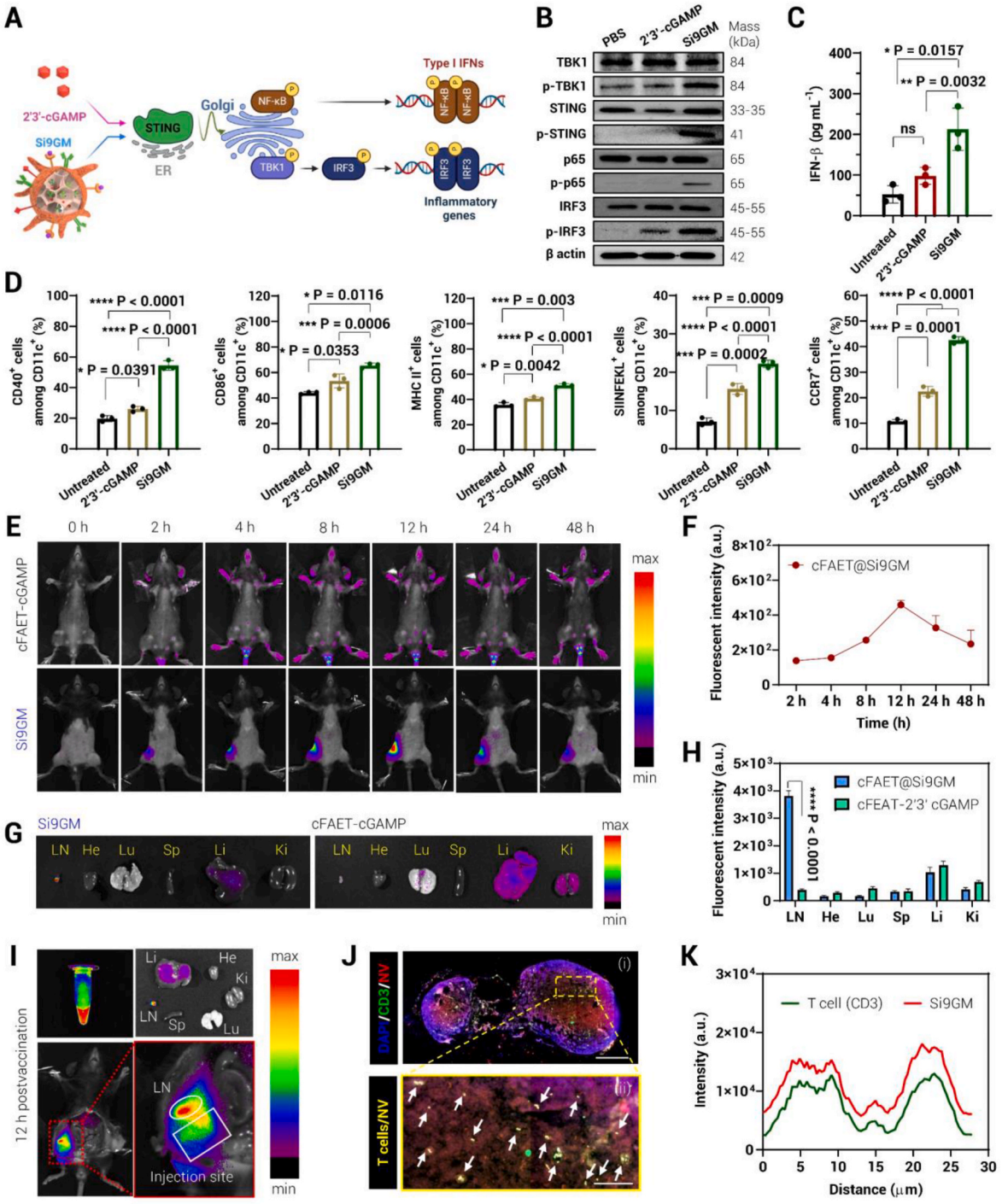


**Fig. 4.** STING pathway activation and biodistribution of Si9GM for DC maturation and T cell interaction. (A) Schematic illustration of STING pathway activation. (B) Western blot assay of 2′3′-cGAMP, and Si9GM inducing TBK1, STING, NF-κB and IRF3 phosphorylation in BMDCs in vitro. (C) ELISA assay of IFN-β produced by 2′3′-cGAMP, and Si9GM in BMDCs in vitro. (D) Flow cytometric analysis of surface biomarkers for DC maturation, antigen cross-presentation, and LN homing ability of Si9GM, free 2′3′-cGAMP in BMDCs. (E) Biodistribution of Si9GM and free 2′3′-cGAMP in C57BL/6 mice within 48 h post subcutaneous injection. (F) Relative fluorescent intensity of inguinal LNs in the Si9GM-treated group with elapsing time post subcutaneous injection. (G) Ex vivo fluorescence imaging of cFAET-labeled 2′3′-cGAMP and cFAET-labeled 2′3′cGAMP@Si9GM distributions in the inguinal LNs and major organs (heart, lung, spleen, liver and kidneys) at 12 h post vaccination. (H) Fluorescent intensity of excised inguinal LNs and main organs (heart, lung, spleen, liver and kidneys) at 12 h after vaccination. (I) Fluorescence images of DiR-labeled@Si9GM sample, excised C57BL/6 mouse at 12 h post-vaccination, excised inguinal LNs, and major organs to analyze LN homing ability of Si9GM originated from the injection site. (J) Immunofluorescent staining of LNs from mice vaccinated with Si9GM, green: $CD3^+$ T cells, red: Si9GM nanovaccine, blue: nuclei, and intensity profile of fluorescence at a specific site in the CLSM image of inguinal LNs; scale bar: (i) 500 μm, (ii) 100 μm. The data is presented as the mean ± standard deviation, with statistical significance determined using one-way ANOVA with Tukey's test (D) or two-way ANOVA with Tukey's test (F). $P > 0.05$ stands for not significant (ns), *$P < 0.05$; **$P < 0.01$; ***$P < 0.001$; ****$P < 0.0001$.

investigated. Impressively, Si9GM induced a higher percentage of CCR7-positive DCs (42.6 ± 1.31 %) compared to those of 2′3′-cGAMP (22.5 ± 1.91 %) (Fig. 4D and S19). Taken together, DC-based nanovaccine Si9GM was well constructed for robust DC activation, LN homing, and enhanced immune response.

### 2.5. Biodistribution and selective recruitment to lymph node of Si9GM

Lymph node has become a key target whereby most immune cells are located in [56]. Therefore, nanovaccines should be effectively delivered to LNs to establish and elicit strong immune responses in cancer immunotherapy [57]. For verification of the LN-homing ability of Si9GM, we used cFAET-labeled 2′3′-cGAMP loaded in Si9GM and free cFAET-labeled 2′3′-cGAMP for subcutaneous injection into mice. The

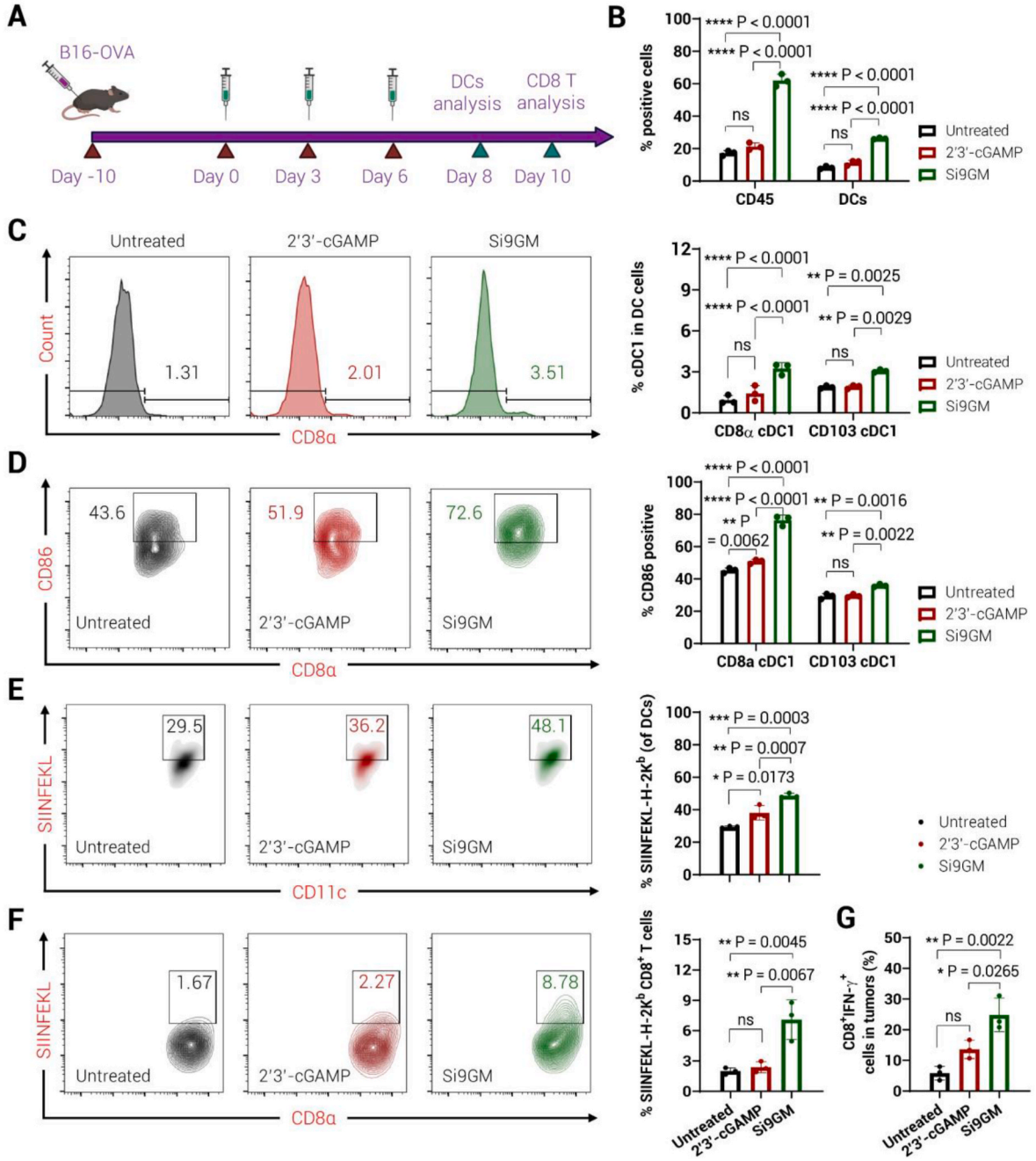


**Fig. 5.** Si9GMs augment the maturation of cDC1s and CD8$^+$ T-cell priming. (A) Schematic illustration of in vivo experiments to analyze the STING pathway activation in cDC1s triggering CD8$^+$ T-cell priming. The 2′3′-cGAMP and Si9GM were administered by s.c. injection, and DCs and T cells were collected at day 8 and day 10 post the first injection, respectively for flow cytometric analysis. (B) Quantitative evaluation of immune cells (CD45$^+$ cells) and DC population (CD11c$^+$ MHC II$^+$) from different treatments. (C) Representative flow cytometric plots of the percentage of cDC1 subsets in DCs: CD8α cDC1 (gated on CD45$^+$ CD11c$^+$ MHC II$^+$) and CD103$^+$ cDC1 (gated on CD45$^+$ CD11c$^+$ MHC II$^+$). (D) Illustrative flow cytometric graphs of costimulatory molecule CD86 and quantification of CD86 percentage in each cDC1 subset. (E) Representative flow cytometric graphs and percentage of antigen SIINFEKL-presented DCs in response to various treatments. (F) Representative flow cytometric graphs and populations of OVA-specific CD8$^+$ T cells. (G) The population of IFN-γ$^+$ CD8$^+$ cells in tumors collected from mice treated with 2′3′-cGAMP and Si9GM compared to the untreated group. The data is presented as the mean ± standard deviation, with statistical significance calculated using one-way ANOVA with Tukey's test (B,C,D) or one-way ANOVA with Tukey's test (E,F). P > 0.05 stands for not significant (ns), *P < 0.05; **P < 0.01; ***P < 0.001; ****P < 0.0001.

fluorescence intensity was surveyed within 2 days. After 12 h, LN and other organs were excised for fluorescence analysis. As presented in Fig. 4E and F, mice treated with dye-labeled Si9GM showed maximal fluorescent intensity at inguinal LN nearby injection site. In contrast, mice injected with free STING agonists represented negligible fluorescent intensity within 2 days, suggesting that Si9GM has a strong tendency to accumulate in inguinal LNs. Correspondingly, FOBI images and quantitative analysis revealed an abundant accumulation of Si9GM in excised inguinal LNs compared to other organs. Meanwhile, only a negligible 2′3′-cGAMP signal was found in excised inguinal LNs of mice treated with free cFAET-labeled 2′3′-cGAMP (Fig. 4G and H, Fig. S20). This is probably due to the existence of CCR7-upregulated DCs treated by Si9GM, which is essential to lymphatic homing of NVs. These results revealed that Si9GM is a potent nanosystem to target STING agonists to this critical lymphoid organ.

Next, the inguinal LNs were collected at 12 h post-vaccination and sectioned for immunofluorescence (IF) staining to examine the interaction between Si9GM NVs and T cells located in LNs. Si9GMs were labeled by 1,1′-dioctadecyl-3,3,3′,3′-tetramethylindotricarbocyanine iodide (DiR) before being vaccinated into mice. After 12 h, mice were excised and the inguinal LNs were collected for the CLSM observation. Based on the presence of overlapping fluorescence between the red (Si9GMs) and green (T cells), we observed that Si9GMs were delivered across LNs and interacted with T cells, indicating the colocalization of Si9GMs and $CD3^+$ T cells (white arrows) (Fig. 4I–K). Therefore, it can be concluded that Si9GMs functioned as artificial antigen-presenting cells (APCs) for DC-T cell interactions.

### 2.6. Si9GM augments cDC1 activation and CD8 T-cell priming

cDC1s are potently adept at presenting both exogenous and endogenous antigens for cross-presentation, as well as promoting T cell activation and proliferation, thereby generating memory and effector T cells [33]. This distinguished function of cDC1s is key to their role in cancer immunotherapy, where they capture antigens and express them to $CD8^+$ T cells after homing to tumor-draining lymph nodes [58,59]. To evaluate the efficacy of Si9GM NVs in selectively recruiting cDC1s for potent antigen presentation and activating $CD8^+$ T cells, we administered subcutaneous injections of Si9GM and 2′3′-cGAMP to mice bearing B16-OVA tumors (Fig. 5A). DCs (including cDC1 subsets) and $CD8^+$ T cells were assessed on days 2 and 4 following the final vaccination. Overall, we observed increased immune cell ($CD45^+$) and DC ($CD11c^+$ MHC $II^+$) populations in tumors of Si9GM-treated mice compared to those of the 2′3′-cGAMP-treated group and the untreated group (Fig. 5B). Two subsets of cDC1 are resident cDC1s ($CD8^+$ cDC1) and migratory cDC1s ($CD103^+$ cDC1). Si9GM-treated mice showed a significant increment in percentage of both $CD8^+$ cDC1s and $CD103^+$ cDC1s compared to the 2′3′-cGAMP-treated group and untreated group. In contrast, the increase in cDC1 population in the 2′3′-cGAMP-treated group was insignificant compared to the untreated group (Fig. 5C, Figs. S21A and C). The expression of co-stimulatory signal CD86 in the cDC1 population was also enhanced in the Si9GM-treated group compared to other groups, potentiating the activation of both $CD8^+$ cDC1s and $CD103^+$ cDC1s (Fig. 5D, Fig. S21B and C).

Notably, the population of DCs with SIINFEKL-presenting H-2Kb MHC-I complexes was also remarkably increased in the Si9GM-treated group (48.7 ± 1.36 %) compared to 2′3′-cGAMP-treated group (38.1 ± 4.43 %) and untreated group (29.4 ± 0.56 %), resulting from more effective antigen cross-presentation in Si9GM-treated mice (Fig. 5E, Fig. S22). Owing to the effective DC activation in the Si9GM-treated group, the percentage of antigen-specific $CD8^+$ T cells was greatly increased compared to the 2′3′-cGAMP-treated group (3-fold) and untreated group (3.5-fold) (Fig. 5F). Correspondingly, the abundant population of antigen-specific $CD8^+$ T cells triggered by Si9GM treatment resulted in significant cytotoxic T cells (IFN-$\gamma^+$ $CD8^+$) compared to other groups (Fig. 5G), promising the potency of Si9GM for generation of an effective strategy in cancer immunotherapy. These results suggest that Si9GM is an effective delivery system for 2′3′-cGAMP to cDC1 cells, enhancing antigen cross-presentation and priming $CD8^+$ T-cells.

### 2.7. Inhibition of melanoma growth in vivo by Si9GM combined with αPD-1 ICB

The antitumor efficacy of Si9GM was investigated in melanoma tumor-bearing mice. We inoculated the B16-OVA cell line into C57BL/6 mice and randomly divided the mice into 6 groups (n = 5 per each group, Table S1). After 7 days of tumor growth (20–30 $mm^3$), mice were subcutaneously injected with various formulations. To investigate whether αPD-1 can effectively combine with Si9GM to trigger a synergistic cancer immunity, αPD-1 antibody (100 μg per dose) was intraperitoneally injected into mice treated with Si9GM after 24 h of nanovaccine administration. The nanovaccine administration was repeated 4 times at intervals of 3 days (Fig. 6A). Tumor growth and body mass were monitored every day. Lymphoid organs (spleens, LNs) and tumors were harvested day 5 following the last vaccination to analyze the impact of various immune cells on tumor suppression (Fig. 6B). At the end of the treatment, the Si9GM-treated group exhibited a remarkable inhibition in tumor growth (Fig. 6C) and a corresponding increase in survival rate (Fig. S23). Meanwhile, mice treated with free 2′3′-cGAMP showed a lower level of significance in tumor inhibition. The SiGM-treated group presented slight efficacy in cancer treatment, suggesting the critical role of CLEC9A-$OVA_{257-264}$ in promoting antigen cross-presentation. Notably, Si9GM therapy combined with αPD-1 resulted in a remarkably reduced tumor volume compared to the untreated group, while αPD-1-only treatment marginally inhibited tumor growth (Figs. S24 and S25). Thus, Si9GM combined with αPD-1 ICB therapy triggered a synergistic effect on antitumor therapy. For more details, the individual tumor growth in each group was presented (Fig. 6D). Similarly, tumor weight and representative photos of tumors in every group at the end of treatment affirmed the anticancer immunity of Si9GM (Fig. 6E and F). The toxicity of nanovaccines was assessed by monitoring changes in body weight and the Haematoxylin & Eosin (H & E) staining of major organs (Figs. S26 and S27). As shown in Fig. S27, there is no significant toxicity observed in the main organs (heart, liver, kidney, spleen) at the end of the treatment. However, we found an increase in the number of inflammatory cells, leading to alveolar wall thickening, in the lungs of mice in the untreated group, as well as in the αPD-1 and 2′3′-cGAMP -treated groups, compared to the SiGM-, Si9GM-, and Si9GM + αPD-1-treated groups. This significant thickening of alveolar walls in the mouse lungs could be attributed to the inflammatory response resulting from the recruitment of immune cells to combat metastatic cancer cells.

To further investigate the antitumor immunity of Si9GM combined αPD-1 ICB, tumors and lymphoid organs (spleens, LNs) were excised for the immune analysis. The representative photos of LNs in each group showed the increased size of LNs in mice treated with Si9GM with or without αPD-1 therapy in comparison with other groups (Fig. S28). Consistent with in vitro data, Si9GM with or without αPD-1 therapy robustly activated DCs in vivo, triggering an abundant population of matured DCs ($CD11c^+$ $CD80^+$ $CD86^+$) for T cell priming. However, no remarkable difference was observed between these two groups that may be attributed to the negligible contribution to the antigen presentation on DCs of ICB. Meanwhile, other groups showed negligible impact on DC maturation compared with the untreated group (Fig. 6G and Fig. S29A). As a key feature of T lymphocyte-mediated immunity, the cytotoxic T cell ($CD3^+$ $CD8^+$) and helper T cell ($CD3^+$ $CD4^+$) populations were determined using flow cytometric analysis. The findings showed that Si9GM significantly enhanced the population of cytotoxic $CD8^+$ T cells and helper T cells, and both fractions were notably enhanced in combination with αPD-1 ICB (Fig. 6H and Figs. S29B, S30). It could be elucidated that αPD-1 antibody contributed to the reduction of T- cell exhaustion [60]. Similarly, the percentage of CD8 T cells and CD4 T cells

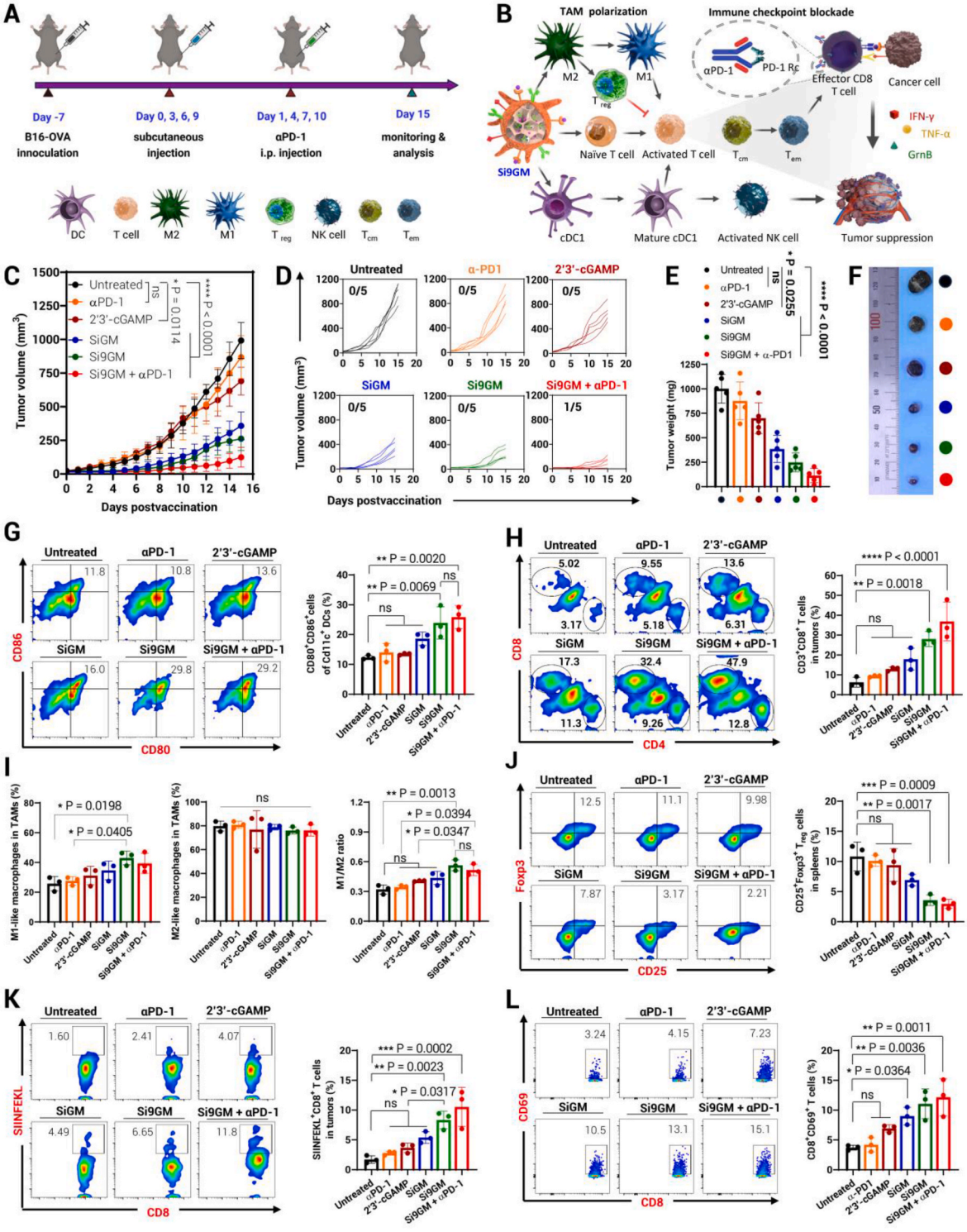


**Fig. 6.** In vivo study of B16-OVA tumor inhibition. (A) Schematic illustration of treatment schedule for melanoma cancer in C57BL/6 mice. (B) Scheme illustrating the role of various immune cells involved in antitumor immunity. (C) Graph presenting tumor volume growth of the B16-OVA tumor-bearing C57BL-6 mice following different treatments over a 16-day period (n = 5). (D) Individual curves of B16-OVA tumor growth of the mice over a 16-day period (n = 5). (E) Excised tumor weight of B16-OVA tumor-bearing mice after 16 days of treatment. (F) Illustrative photos of tumors in each group at the end of treatment. (G) Representative flow cytometric graphs and proportions of mature DCs ($CD11c^+$ $CD80^+$ $CD86^+$) in spleens at the end of the schedule. (H) Illustrative flow cytometric graphs and proportions of T cells in tumor tissues observed on day 7 after the last vaccination. (I) The proportions of M1-like, M2-like macrophages in TAMs and the M1/M2 ratio in tumor tissues observed on day 7 after the last vaccination. (J) Illustrative flow cytometric graphs and percentages of regulatory $CD4^+$ T cells in spleens. (K) Illustrative flow cytometric graphs and proportions of $SIINFEKL^+$ $CD8^+$ T cells in tumors. (L) Illustrative flow cytometric graphs and percentages of activated T cells ($CD3^+$ $CD8^+$ $CD69^+$) in LNs at day 3 after the last vaccination. (M) Illustrative flow cytometric graphs and proportions of $SIINFEKL^+$ $CD11c^+$ DC cells in spleens at day 3 after the last vaccination. (N) Illustrative flow cytometric graphs and proportions of tumor-infiltrated $IFN\gamma^+$ $NK1.1^+$ NK cells. (O) Representative flow cytometric graphs and percentages of tumor-infiltrated $IFN\gamma^+$ $CD8^+$ T cells in tumors on day 7 after the last vaccination. (P) Illustrative flow cytometric graphs and percentages of tumor-infiltrated $GrnB^+$ $CD8^+$ T cells in tumors on day 7 after the last vaccination. (Q) Illustrative flow cytometric graphs and proportions of $CD8^+$ T cells, memory effector

T cells, and memory central T cells in tumors. (R) Immunofluorescent images of tumors stained by CD8 antibody, DAPI. (S) Immunofluorescent images of tumors stained by Ki67 antibody, DAPI. (T) ELISA assay of inflammatory cytokine levels (IFN-γ, TNF-α, IL-2, IL-6, and IFN-β) in serum collected from B16-OVA tumor-bearing mice at 72 h post final vaccination. The data is presented as the mean ± standard deviation, with statistical significance determined using one-way ANOVA with Tukey's test. $P > 0.05$ stands for not significant (ns), *$P < 0.05$; **$P < 0.01$; ***$P < 0.001$; ****$P < 0.0001$.

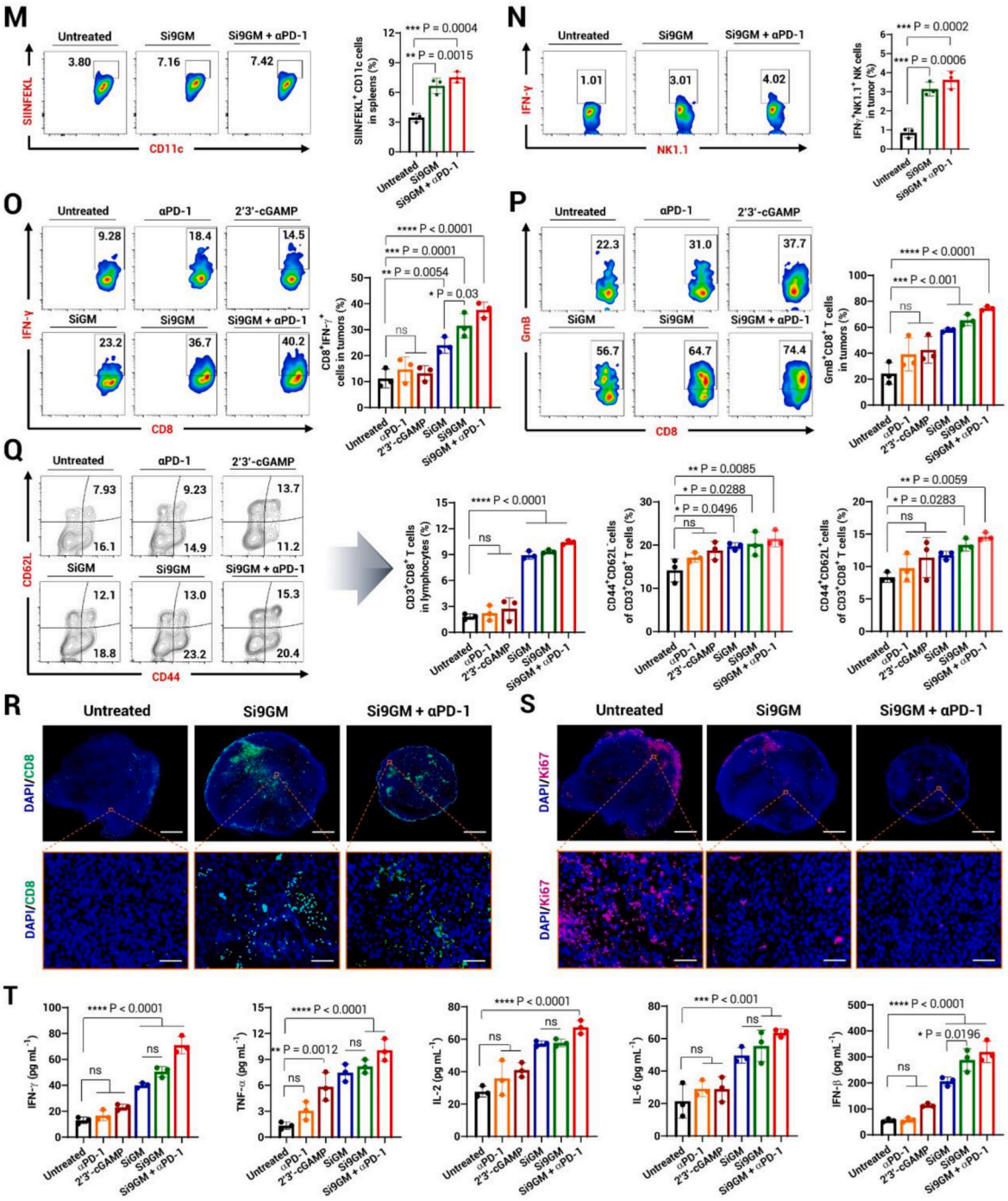


**Fig. 6.** (*continued*).

in spleens also increased in the Si9GM-treated group with or without ICB therapy (Fig. S31). In the TME, assessing the ratio of M1-like to M2-like tumor-associated macrophages (TAMs) is essential for controlling inflammatory responses and tissue damage [61]. The treatment generated the dominant pro-inflammatory M1-like TAMs (a higher M1/M2 ratio) in the TME, promoting T cell immune responses and strengthening T and NK cells through secreted immuno-stimulatory cytokines (IL-6, TNF-α, …) [62]. In contrast, the treatment produced a lower M1/M2 ratio reflects an increment in immune suppressive M2-like TAMs, attenuating antitumor immunity, and facilitating tumor chemoresistance. To determine whether Si9GM therapy can positively regulate macrophage polarization due to the presence of STING agonist as previously reported [31,32], we stained singlet tumor cells excised at the last day of the treatment for flow cytometry analysis. Then, the populations of M2-like macrophages ($CD11b^+$ $F4/80^+$ $CD206^+$) and M1-like-macrophages ($CD11b^+$ $F4/80^+$ $CD86^+$) were examined and the M1/M2 ratio was calculated. There was a robust polarization from the M2 population to the M1 population after Si9GM treatment (Fig. 6I and Fig. S29C).

Consistent with that data, the average M1/M2 ratio decreased from 0.56 ± 0.06 in the Si9GM-treated group to 0.32 ± 0.05 in the untreated group, indicating the ability of Si9GM to regulate an immune response for effective anti-tumor immunity. Interestingly, we found a slight decrease of M1/M2 ratio in the combination of Si9GM and αPD-1 ICB compared with only Si9GM therapy. This could be attributed to the combination of αPD-1 and Si9GM treatment, which may induce the expression of αPD-1 antibodies in TAMs) weakening their cytotoxic activity against tumor cells. This can result in the promotion of immunosuppressive M2-like TAMs, thereby enhancing the immune evasion mechanisms of tumor cells, and affecting the TME [63]. Notably, M2-like macrophages secreted some anti-inflammatory cytokines that can inhibit T cells and NK cell activation but induce regulatory T cells (Tregs) [64], enhancing the immunosuppressive environment. In addition, Treg infiltration with a significant number of cells into tumors induces tumor progression and a poor prognosis due to immune tolerance/escape of Tregs cells against antitumor immune responses [65]. For verification of tumor suppression-induced Tregs, we examined the role of Si9GM in regulating Tregs in comparison with other groups. As shown in Fig. 6J and Fig. S29D, the administration of Si9GM led to a decrease in the infiltration of immunosuppressive regulatory Tregs ($CD3^+$ $CD4^+$ $CD25^+$ $Foxp3^+$, 3.57 ± 0.89 %) in the TME compared to the untreated group (10.82 ± 2.40 %), consistent with the tumor inhibition observed with Si9GM. The addition of αPD-1 ICB slightly decreased the Treg population, while other treated groups did not reveal a similar impact. Our results emphasized that Si9GM-immunized mice displayed a decreased Treg population, especially in combination with αPD-1, thus reversing the immunosuppressive TME for effective cancer immunotherapy.

Furthermore, we investigated how efficient antigen peptides were processed and presented to $CD8^+$ T cells. We examined the population of SIINFEKL-specific $CD8^+$ T cells in excised tumors, LNs, and spleens (Fig. 6K, Figs. S32 and S33). The obtained data showed a significant increment in SIINFEKL-specific $CD8^+$ T cell population in groups treated with Si9GM and Si9GM + αPD-1 ICB with 8.34 ± 1.48 % for the former and 10.55 ± 3.27 % for the latter. In contrast, mice vaccinated by free 2′3′-cGAMP or via intraperitoneal (i.p.) administration of αPD-1 did not generate a significant percentage of SIINFEKL-specific $CD8^+$ T cells in comparison to untreated mice. Furthermore, we checked the activation of $CD8^+$ T cells ($CD3^+$ $CD8^+$ $CD69^+$). We found a significant increase in the population of activated $CD8^+$ T cells in mice treated by Si9M and Si9GM + αPD-1. Other treatments (αPD-1, 2′3′-cGAMP, SiGM) did not robustly promote the T cell activation (Fig. 6L). Furthermore, the population of SIINFEKL-expressed $CD11c^+$ DCs in spleens and LNs was also determined between untreated mice and mice immunized with Si9GM and Si9GM + αPD-1. An abundant accumulation of SIINFEKL-expressed $CD11c^+$ DCs was consistently revealed in spleens after both therapies compared to the untreated group (Fig. 6M and Fig. S34). The population of IFN-γ-secreting NK cells increased after Si9GM vaccination, promising NK cell-induced tumor rejection (Fig. 6N). The essential role of Si9GM nanovaccines in activating NK cell function for antitumor immunity could be elucidated by the type I IFN-induced IFNAR1 pathway triggered by the STING stimulation in DCs [66]. Importantly, IFN-γ and granzyme B secreted by activated $CD8^+$ T cells were also evaluated in tumor tissues at the end of the therapy (Fig. 6O and P). The abundant increase of secreted IFN-γ on $CD8^+$ T cells was observed in Si9GM therapy without or with αPD-1 blockade over 2.8- and 3.4-fold higher, respectively, than in the untreated group, demonstrating enhanced antitumor immune response in these groups (Fig. 6O). To evaluate the long-term immune response, the populations of effector memory T cells ($T_{EM}$, $CD3^+$ $CD4^+$ $CD44^+$ $CD62L^-$) and central memory T cells ($T_{CM}$, $CD3^+$ $CD4^+$ $CD44^+$ $CD62L^+$) were examined. We found that the frequency of $T_{EM}$ and $T_{CM}$ increased significantly in the group treated with SiGM, Si9M, or Si9GM + αPD-1 compared to the untreated group, indicating long-term protective immunity following vaccination (Fig. 6Q and Fig. S29E).

In addition, tumor tissues from the untreated group, Si9GM-treated group, and Si9GM combined with αPD-1-treated group were sectioned for hematoxylin and eosin (H&E) staining to observe tumor inhibition (Fig. S35). IF staining was also performed using nuclear protein Ki67 and CD8 antibodies to investigate cell proliferation and T cell recruitment, respectively. A massive presence of $CD8^+$ T cells was also observed in those treated groups, complying with the flow cytometric data reported above (Fig. 6R). The IF staining further confirmed the inhibition of tumor cell proliferation in mice treated with Si9M and Si9GM + αPD-1 with negligible presence of Ki67 proteins compared to the untreated group (Fig. 6S).

Furthermore, samples of serum were collected from blood of mice in 6 groups and used for ELISA analysis (Fig. 6T). The data showed all upregulation of secreted cytokines (IFN-γ, TNF-α, IL-6, IL-2) from Si9GM with or without αPD-1 therapy, consistent with the above accumulating results, indicating the effectiveness of Si9GM vaccination in combination with αPD-1 in treating melanoma cancer. Notably, the concentration of IFN-β protein in serum samples of Si9GM-treated mice with or without αPD-1 therapy was higher compared to the untreated group and 2′3′-cGAMP-treated group, confirming the massive production of type I IFN through STING activation after Si9GM vaccination.

### 2.8. Si9GM in lung metastasis inhibition and the role of NK cells

Despite significant advances in nanovaccines in cancer immunotherapy, the challenge of metastasis from the primary tumor to distant organs remains [67]. In this experimental model, we examined the capacity of Si9GM in combination with αPD-1 blockade in inhibiting metastasis to the lungs. C57BL/6 mice were intravenously injected with B16-OVA tumor cells two days before vaccination and immunized with various treatments on days 0, 3, 6, and 9 (Fig. 7A). Lungs were collected on day 20 for analysis. As shown in Fig. 7B, there was an extensive spread of metastasis focus in the lungs of untreated, αPD-1-treated, and 2′3′-cGAMP-treated mice. In contrast, vaccination with SiGM or Si9GM without and with ICB had a significant inhibitory impact on lung metastatic tumor surveillance. Lung weights in untreated, αPD-1-, and 2′3′-cGAMP-treated groups were remarkably higher than those in SiGM or Si9GM without and with ICB groups due to the abundant formation of metastatic nodules in the former (Fig. 7C). For further verification of metastasis formation in lung tissues, we harvested lungs for H & E staining. As illustrated in Fig. 7D, massive tumor foci were observed in untreated, αPD-1-, and 2′3′-cGAMP-treated groups, but no significant hallmark of lung metastasis was found in the other groups.

Next, we investigated the role of immune cells in lung metastasis inhibition by flow cytometry of digested lung tissues at the endpoint. NK and T cells, the two most potent immune effector cells, were taken into the examination. As shown in Fig. S36, there was no distinct difference between the $CD4^+$ or $CD8^+$ T cell population in untreated and Si9GM-treated mice. Consistently, the percentage of $IFN\gamma^+$ $CD8^+$ T cells in these groups was similar. Of note, the population of IFN-γ-secreted NK cells was incredibly boosted in Si9GM with or without αPD-1 blockade compared to other groups, indicating a critical antitumor function of NK cells in preventing the spread of cancer cells to distant organs (Fig. 7E and F). The body weight of mice and the survival rate in each group were recorded (Figs. S37 and S38).

To further identify the contributions of NK and T cells, we compared the control groups (G1, G2) with two other groups (G3, G4) in which NK and $CD8^+$ T cells were diminished by antibodies in mice received Si9GM + αPD-1 treatment (Fig. 8A). As shown in Fig. 8B, effective inhibition of lung metastatic seeding of B16 melanoma cells was observed in the G4 group (Si9GM + αPD-1 + CD8α depletion) compared to the G1 group (untreated mice), G2 group (IgG isotype-treated mice) and G3 group (Si9GM + αPD-1 + NK cells depletion). Notably, the G3 group showed a significant quantity of lung metastatic foci that is like those of G1, and G2 group. In contrast, the depletion of $CD8^+$ T cells in the G4 group did not impair the effectiveness of the treatment, with a remarkable

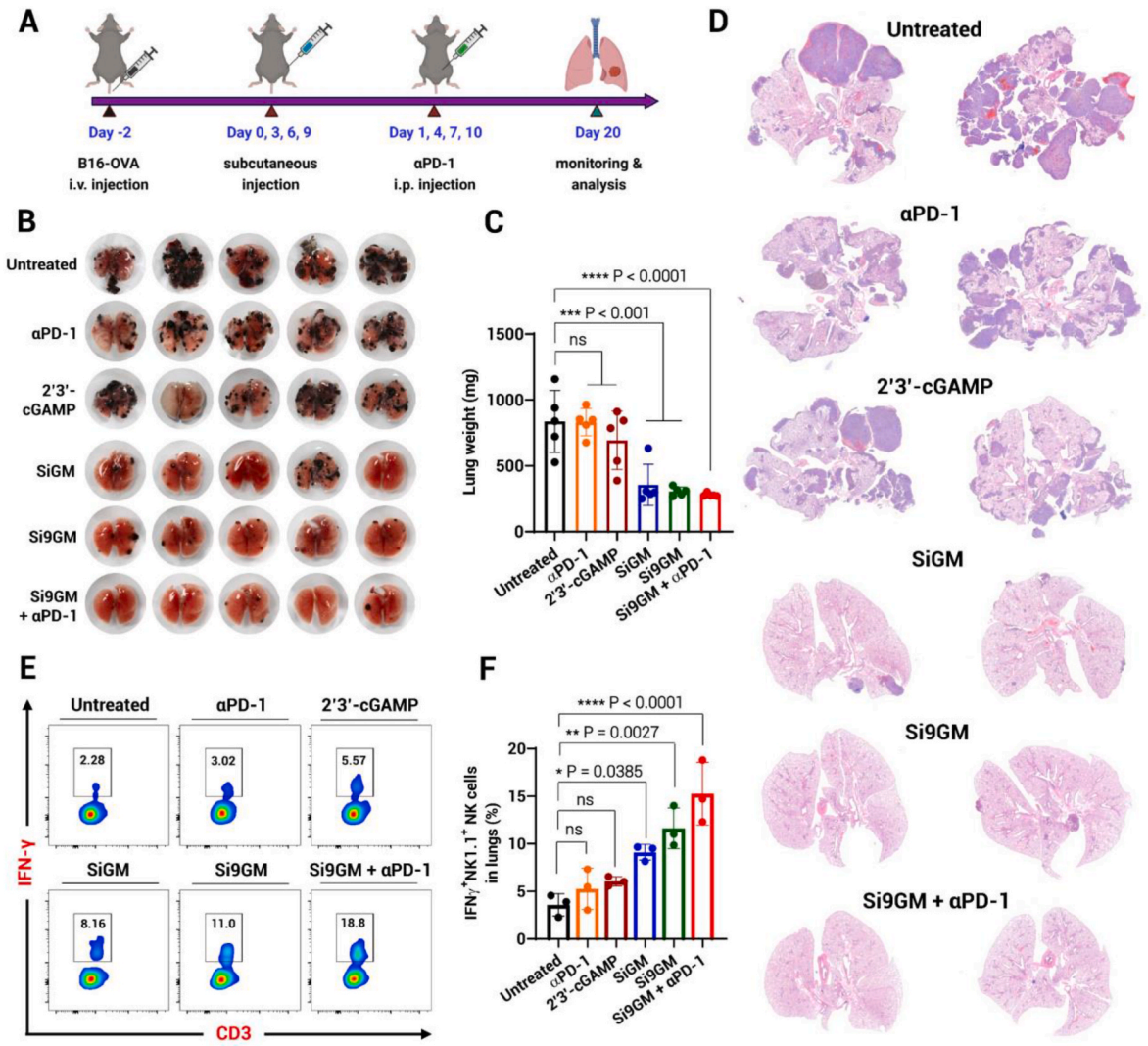


**Fig. 7.** Inhibition of lung metastasis of Si9GM combined with αPD-1 ICB in melanoma cancer. (A) Schematic illustration of lung metastasis inhibition treatment. (B) Excised lungs in all groups at the end of treatment. (C) Weight of excised lungs at the end of treatment. (D) H & E staining of excised lungs. E, F) Illustrative flow cytometric plots and proportions of IFNγ$^+$ NK1.1$^+$ cells in lungs. All data are presented as the mean ± standard deviation, with statistical significance calculated via one-way ANOVA with Tukey's test. P > 0.05 stands for not significant (ns), *P < 0.05; **P < 0.01; ***P < 0.001; ****P < 0.0001.

decrease in the number of lung metastatic seeds (Fig. 8B). In addition, H & E staining of lung tissues at the endpoint verified the presence of metastatic foci in B16 melanoma cells (Fig. 8C). Consistently, the lung weight was higher in G1, G2, and G3 than in G4 (Fig. 8D), highlighting the prominent role of NK cells over CD8$^+$ T cells in prevention of lung metastasis in B16 melanoma cancer cells. These findings could be attributed to the abundant localization of NK cells in peripheral blood compared to other organs (lung, skin, liver, kidney, and bone marrow), instantly reducing circulating cancer cells post i.v. injection [68]. Furthermore, the underlying mechanism of NK cells in metastasis prevention is supposed to be triggered by STING pathway activation in cDC1s post-Si9GM vaccination. In detail, Si9GMs internalize dendritic cells (selectively target in cDC1s), following the release of 2′3′-cGAMP for STING stimulation. Subsequently, the type I interferons produced from DCs are transferred to NK cells by expression of interferon-α/β receptor (IFNAR) on NK cells. As a result, interferon alpha/beta receptor 1 (IFNAR1) signaling in NK cells promoted NK cell function, activation and generated cytotoxic cytokines like IFN-γ for metastasis rejection [66]. Therefore, in the absence of NK cells in the G3 group, the number of lung metastatic foci was slightly increased compared to G1, G2 group. Impressively, the presence of an increased population of migratory CD103 cDC1s was observed in Si9GM + αPD-1-treated mice, contributing to the inhibition of lung foci growth (Fig. 8E). In addition, a larger increment in IFNγ-NK cells was observed in the G4 group compared to the G1 group (2.9-fold) (Fig. 8F). Meanwhile, there was no significant increase in T cell population between G1 and G2 groups (Fig. 8G). Taken together, these findings demonstrate that NK cells and CD103 cDC1s might play a prominent role in evading the seeding of lung metastasis compared to CD8$^+$ T cells in B16 melanoma cancer cells [69].

## 3. Conclusion

In this study, we proposed an attractive DC-based nanovaccine selectively targeting cDC1 to augment the STING pathway activation and type I IFN production profile for effective cancer vaccination immunotherapy. Leveraging the unique ability of cDC1s in antigen cross-presentation and cytotoxic T lymphocyte activation, we developed a novel nanovaccine formulation in which large pore dendrimer-like silica NPs with hierarchical center-radial pores, delivering distinct sizes of αCLEC9A-OVA$_{257\text{-}264}$ conjugate and STING agonist, were coated with BMDC-derived membranes containing CLEC9A antibodies and antigen peptides. αCLEC9A-conjugated DC membranes drive nanovaccine to cDC1s, while αCLEC9A-OVA$_{257\text{-}264}$ can avoid lysosomal degradation and the loss of prematurely released antigens. Notably, 2′3′-

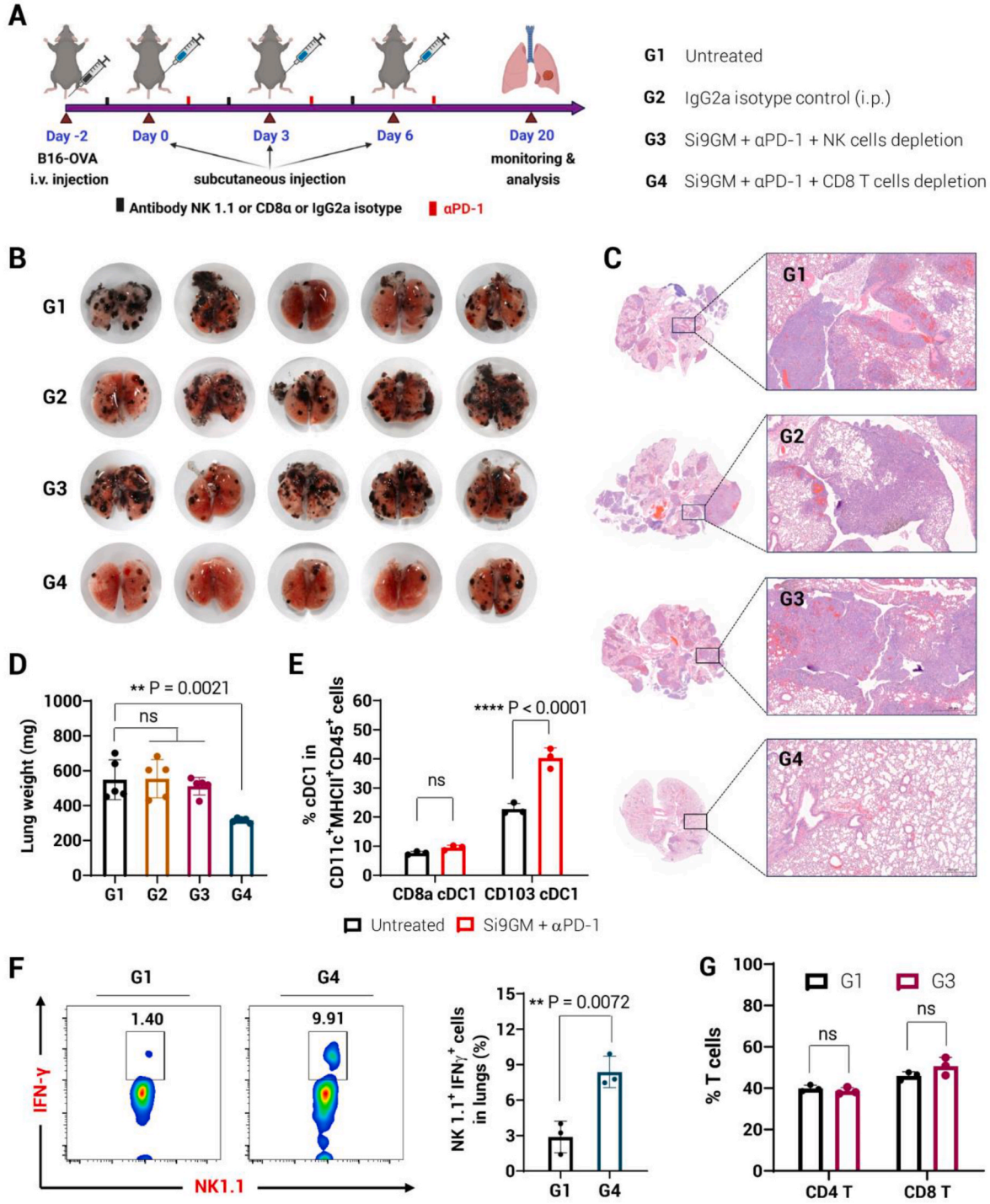


**Fig. 8.** Investigation of the role of immune cells in lung metastasis prevention. (A) Schematic overview of lung metastasis inhibition in the depletion of NK cells (G3) and CD8 T cells (G4) compared to the untreated group (G1), and IgG2a isotype injection (G2). (B) Excised lungs at the end of treatment. (C) H & E staining of excised lungs in G1, G2, G3, and G4. (D) Weight of excised lungs in G1, G2, G3 and G4 group. (E) Analysis of the population of cDC1s subsets ($CD8\alpha^+$ cDC1), ($CD103^+$ cDC1) in lungs (gated on $CD45^+$ $CD11c^+$ $MHCII^+$) by flow cytometry. (F) Illustrative flow cytometric graphs and proportions of $IFN\gamma^+$ $NK1.1^+$ cells in lungs by flow cytometric evaluation. (G) Examination of T cell population in lungs at the end of treatment. Data are presented as the mean ± standard deviation, with statistical significance calculated via one-way ANOVA with Tukey's test (D), or two-way ANOVA with Tukey's test (E,G), or two-tailed Student's t-test (F). $P > 0.05$ stands for not significant (ns), *$P < 0.05$; **$P < 0.01$; ***$P < 0.001$; ****$P < 0.0001$.

cGAMP stimulates type I interferons, leading to robust $CD8^+$-specific antigen cross-presentation and effective immune response. The DC-based nanovaccine Si9GM synergized with αPD-1 blockade to elicit effective inhibition of B16-OVA tumor progression and metastasis without apparent side effects. Impressively, Si9GM with αPD-1 ICB can regulate macrophage polarization, inhibit Tregs, and initiate enduring immunological memory against tumor cells. The potency of Si9GM addresses existing disadvantages of live cell-based vaccines, such as limited immunogenicity, risk of pathogenicity, storage challenges, and inherits the advantages of DC-based vaccines. Overall, this work presents the first time that the formulated nanovaccines, combining porous inorganic nanoparticles and APC-derived membranes, can selectively

target the cDC1 subset to evoke robust STING activation and promote potent antigen cross-presentation, thereby facilitating efficient personalized cancer immunotherapy.

## 4. Experimental section

### 4.1. Materials and methods

The 2′3′-cGAMP was purchased from MedChemExpress (Monmouth Junction, NJ, USA). Cyclic (8- (2- [fluoresceinyl]aminoethylthio)- guanosine- (2′,5′)- monophosphate-adenosine- (3′,5′)- monophosphate) sodium salt (denoted as cFAET-labeled 2′3′-cGAMP) was purchased from BioLog Inc. (Hayward, CA, USA). The $OVA_{257-264}$ peptide fragment and FAM-labeled $OVA_{257-264}$ were purchased from Anaspec (Fremont, CA, USA). Lipopolysaccharides from Escherichia coli O111:B4 (cat. no. L3024), (3-aminopropyl) triethoxysilane (APTES), cetyltrimethylammonium bromide (CTAB), branched polyethylenimine (0.8 kDa), Tetraethyl orthosilicate (TEOS), 2-iminothiolane hydrochloride (Traut's reagent), succinic anhydride (SA), and 4-(N-maleimidomethyl) cyclohexane-1-carboxylic acid 3-sulfo-N-hydroxysuccinimide ester sodium salt (sulfo-SMCC) were purchased from Sigma-Aldrich. Neuro-DiO was purchased from Biotium (Fremont, CA, USA). 1,1′-Dioctadecyl-3,3,3′,3′-tetramethylindocarbocyanine perchlorate (cat. no. D3911), Hoechst 33342 (cat. no. H1399), and LysoTracker™ Red DND-99 (cat. no. L7528), FITC Annexin V/Dead Cell Apoptosis Kit (cat. no. V13242) were purchased from Invitrogen (Thermo Fisher Scientific, MA, USA). Dynabeads® Mouse T-Activator CD3/CD28 (cat. no. 11456D) was purchased from Gibco (Thermo Fisher Scientific, MA, USA). Recombinant murine GM-CSF protein (cat. no. 315-03), mouse IL-2 recombinant protein (cat. no. 212-12-20UG) were purchased from PeproTech (Thermo Fisher Scientific, MA, USA). Recombinant mouse IL-4 protein (cat. no. 51084-MNAE) was purchased from Sino Biological (Beijing, China). Human FLT3-ligand (research grade) was purchased from Miltenyi Biotec (North Rhine-Westphalia, Germany). ELISA kits of IL-6, IL-2, TNF-α, IFN-γ were purchased from Invitrogen (Thermo Fisher Scientific, MA, USA). LEGEND MAX™ Mouse IFN-β ELISA kit (cat. no. 439407) and MojoSort™ Mouse CD8 T Cell isolation kit (cat. no. 480008), Alexa Fluor® 488 Goat anti-hamster (Armenian) IgG antibody (cat. no. 405508), CFSE cell division tracker kit (cat. no. 423801) were purchased from BioLegend (San Diego, CA, USA). All antibodies used for Western blot, in vivo experiments, and flow cytometric analysis were listed in Tables S2–S4.

### 4.2. Cell cultures and animals

DC2.4 dendritic cell line used for the in vitro study was purchased from Millipore and B16-OVA cell line used for the in vivo study was purchased from the American Type Culture Collection. DC2.4 and B16-OVA cells were cultured in RPMI and DMEM medium, respectively, both containing 10 % heat inactivated-FBS (HI-FBS), 1 % antibiotics (penicillin−streptomycin, 10,000 U $mL^{-1}$), and 50 μM mercaptoethanol-2 in a humidified atmosphere containing 5 % $CO_2$ at 37 °C. BMDCs and cDC1s were isolated from femurs and tibias of 7-8-week-old C57BL/6 mice and then stimulated with high-glucose RPMI media containing GM-CSF and IL-4 for the generation of BMDCs and with FLT3L for the generation of cDC1s.

C57BL/6 mice (6-week-old females, 7-week-old males) were ordered from ORIENT BIO (Seongnam, South Korea). OT-I mice were kindly provided by Prof. Yong Taik Lim (Sungkyunkwan University, Korea). The mice were housed under conditions with a regulated 12-h light and 12-h dark cycle, with lights turning on at 8:00 a.m.

### 4.3. Synthesis of hierarchical large-pore amino-functionalized silica nanoparticles

For the loading of high-molecular-mass proteins like αCLEC9A-$OVA_{257-264}$ conjugates, dendrimer-like large-pore silica nanoparticles with hierarchical pores were synthesized with some modifications [41]. For details, DHPSi-$NH_2$ NPs were formulated based on the mechanism of the quasi-emulsion nanodroplet method. Firstly, 70 mL of deionized water was added to a 125-mL amber glass bottle with a stir bar. After that, a mixture of diethyl ether (15 mL) and ethanol (5 mL) was dropped into the water using a syringe pump (pumping speed: 2000 μL $min^{-1}$) while stirring at 1050 rpm. Subsequently, 500 mg of CTAB was added, followed by the dropwise addition of 800 μL of TEA. After 30 min, a mixture of TEOS and APTES in the ratio of 1.5 mL–60 μL was dripped into the above mixture, and the reaction lasted for 3.5 h before adding 1 mL of HCl to terminate the base-catalyzed reaction.

Subsequently, raw products were collected by centrifugation at 8200 rpm for 12 min and washed in ethanol: DW (2:1, v/v) before being dispersed into ethanol. For further purification, as-prepared DHPSi-$NH_2$ NPs were dispersed in 100 mL ethanol and then sonicated in a bath for 30 min before probe sonication (20 min, 2s ON-2s OFF). After that, consecutive centrifugation cycles at 2000 rpm, 2500 rpm, 3000 rpm, 3500 rpm, 4200 rpm, and 6200 rpm (3 min for each cycle) were conducted to remove large NPs [70]. The final supernatant was washed three times with ethanol to obtain DHPSi-$NH_2$. The CTAB templates were extracted by refluxing (70 °C for 24 h) in 12.5 % volume of concentrated HCl in ethanol. The final DHPSi-$NH_2$ NPs were obtained by centrifugation at 12,500 rpm for 15 min and washed with ethanol three times before further conjugation steps.

### 4.4. Synthesis of DHPSi-PEI

Next, 5 mg of DHPSi-$NH_2$ was dispersed in 2 mL of DMF and then put in an ultrasonic bath for 10 min. After that, 45 mg of succinic anhydride was dissolved in 0.5 mL of DMF and then added to the as-prepared DHPSi-$NH_2$ solution. The pH was turned to basic conditions by adding 40 μL of TEA, and the mixture was stirred at 600 rpm for 12 h at RT. The resulting DHPSi-COOH NPs were washed three times in a mixture of ethanol: DW (2:1, v/v). Subsequently, DHPSi-COOH was conjugated to EDC.HCl and NHS in DMF for 30 min before adding branched PEI (0.8 kDa, 100 mg $mL^{-1}$). The final product DHPSi-PEI was purified by washing three times in a mixture of ethanol: DW (2:1, v/v).

### 4.5. Generation of cDC1 from bone marrow

For the generation of cDC1s, femurs and tibias from 7-8-week-old mice were isolated. Bone mesenchymal stem cells (BMSCs) were obtained from cavities of bone marrows. Bone marrow-derived stem cells (BMSCs) were isolated from the femurs and tibias of 7-8-week-old male C57BL/6 mice. Subsequently, BMSCs were flushed from the marrow cavities using a needle and RPMI-1640 medium containing 10 % heat-inactivated fetal bovine serum (HI-FBS), 1 % antibiotics (penicillin-streptomycin, 10,000 U $mL^{-1}$), and 50 μM 2-mercaptoethanol (referred to as 10 % HI-FBS RPMI-1640). The cells were then lysed using red blood cell (RBC) lysis buffer and washed in HBSS without calcium. After RBC lysis, BMSCs were seeded on 6-well plates at a cell density of $1.5 \times 10^6$ cells/well and then stimulated in 10 % HI-FBS RPMI-1640 supplemented with 200 ng $mL^{-1}$ FLT3L. One-half of the media volume was replaced at day 4 and day 8, and the non-adherent cDC1s were harvested at day 11 [71].

### 4.6. Generation of bone marrow-derived BMDC nanovesicles

BMSCs were extracted from femurs and tibias of male C57BL/6 mice (7-8-week-old). Additional BMSCs were flushed from marrow cavities using a needle with RPMI-1640 containing 10 % heat inactivated-FBS (HI-FBS), 1 % antibiotics (penicillin−streptomycin, 10,000 U $mL^{-1}$), and 50 μM mercaptoethanol-2 (denoted as 10 % HI-FBS RPMI-1640). These cells were lysed by RBC lysis buffer and washed in HBSS without $Ca^{2+}$. The collected BMSCs were stimulated in as-prepared 10 % HI-FBS

RPMI-1640 containing 20 ng $mL^{-1}$ of GM-CSF and 20 ng $mL^{-1}$ of IL-4 and then seeded in non-TC petri dishes at a cell density of $0.3 \times 10^6$ cells $mL^{-1}$. After 3 days of incubation, 12.5 mL of media was added to each cultured Petri dish. At day 6, one-half of the media was replaced with new media; the non-adherent cells were harvested at day 8 for LPS activation (1 μg $mL^{-1}$) for 24 h [72].

After LPS activation, immature BMDCs were collected, and the BMDC-derived membranes were extracted by Mem-PER™ Plus Membrane Protein Extraction Kit following the manufacturer's instruction. In detail, BMDCs were washed with cell wash solution before adding to cell permeabilization buffer (including 1X proteinase inhibitor cocktail). Cell suspensions were incubated on ice for 30 min before shaking at 4 °C for 1 h. Subsequently, cell suspensions were centrifuged at 800 g for 5 min to eliminate cell debris. After that, supernatant was collected and centrifuged at 27, 000 g for 30 min 4 °C to obtain cell membranes. After the last centrifugation cycle of washing, BMDC membranes were lyophilized and stored at −80 °C for further use.

### 4.7. Preparation of αCLEC9A @DC-$OVA_{257-264}$

To load $CD8^+$ T cell-specific antigen fragments $OVA_{257-264}$ onto MHC-I molecules of BMDC membranes, BMDCs (2 mg $mL^{-1}$) and $OVA_{257-264}$ were incubated in 0.2 M sodium acetate (pH 5.2) in PBS (v/v = 1:1) for 45 min at RT. Subsequently, the pH was adjusted to neutral (pH ~ 7–7.4) by Tris buffer (2 M, pH 11), and the mixture was incubated on ice for 45 min to stabilize antigen peptide-MHC I complex. DC-$OVA_{257-264}$ membranes were centrifuged at 27,237×*g* for 20 min at 4 °C and then were rinsed twice to remove unloaded peptides. These membranes then were incubated with Traut's reagent in PBS pH 8 and washed with Tyrode's buffer for 30 min at RT; the unreacted Traut's reagents were removed by centrifugation. Meanwhile, αCLEC9A antibodies were conjugated with sulfo-SMCC in PBS (pH 7.4, 2.5 mM EDTA) for 1 h at RT, and the excess cross linkers were eliminated by Zebra Spin Desalting Columns 7K MWCO. After that, the as-conjugated DC-$OVA_{257-264}$ and αCLEC9A were mixed and incubated at 4 °C overnight. αCLEC9A @DC-$OVA_{257-264}$ membranes were collected by centrifugation at 27,237×*g* for 20 min at 4 °C and then were washed to remove unconjugated antibodies.

### 4.8. Preparation of αCLEC9A-$OVA_{257-264}$ conjugates

In short, purified antibodies CLEC9A (CD370) and a rat IgG2a isotype control (C1.18.4) were functionalized with 2 equivalents of sulfo-SMCC in PBS pH 8 for 1 h at RT. Meanwhile, endotoxin-free $OVA_{257-264}$ peptide fragments were conjugated with 2 equivalents of Traut's reagent in PBS pH 7.4. Antibodies were desalted over Zebra Spin Desalting Columns 7K MWCO. After that, 6 equivalents OVA were added to antibodies while stirring for 2 h at RT before purification by desalting [73].

### 4.9. Preparation and characterization of Si9GM

DHPSi-PEI NPs were dispersed in endotoxin-free DW at a concentration of 2 mg $mL^{-1}$, followed by adding 2′3′-cGAMP (50 μg per 1 mg of DHPSi-PEI NPs) and stirring at 500 rpm for 30 min at RT. After that, αCLEC9A-$OVA_{257-264}$ conjugates were added for loading at 4 °C overnight. After removing excess cargo by centrifugation, (2′3′-cGAMP and αCLEC9A-$OVA_{257-264}$ conjugate)-loaded DHPSi-PEI NPs (denoted as Si9G) were coated by αCLEC9A@DC-$OVA_{257-264}$. In detail, DHPSi-PEI NPs was dispersed in 10 mM phosphate buffer pH 7.4 (2 mg $mL^{-1}$) before adding in BMDC-derived solution (2 mg $mL^{-1}$) for sonication in 7 min. The as-prepared membrane-coated NPs were then washed twice with phosphate buffer to obtain Si9GM. Subsequently, size and morphology were investigated by TEM.

### 4.10. Western blotting

The proteins in BMDC lysate, BMDC membranes, and BMDCs were extracted in RIPA buffer containing Protease Inhibitor Cocktail (PIC) in which PIC: RIPA = 1:100 (v/v). The extraction occurred at 4 °C for 30 min under shaking. The protein concentrations were evaluated by BCA assay. For denaturation, proteins were heated at 95 °C for 8 min. Subsequently, a comparative amount of proteins was loaded into each well of 10 % or 12 % SDS polyacrylamide gel depending on the analyzed protein size. Electrophoresis was carried out at 70 V for 30 min and then 100 V for 70 min, followed by protein transfer onto a polyvinylidene fluoride (PVDF) membrane (100 V, 120 min). Following a 1-h blocking step with 5 % nonfat milk at RT, the PVDF membranes were then immersed with specific primary antibodies (Table S2) at 4 °C for 12 h under shaking at 30 rpm. After washing with 1 % Tween-20 of Tris-Buffered Saline solution (TBS-T 1 %), the membranes were then immersed with HRP-conjugated secondary antibody for 1 h at RT. Subsequently, the membranes were washed three times by TBS-T 1 % and then immersed in Pierce™ ECL Western Blotting Substrate for 5 min on the shaker. Subsequently, the protein bands in PVDF membranes were observed by a ChemiDoc Imaging System (Bio-Rad).

### 4.11. Coomassie protein electrophoresis

All the proteins in BMDC lysate and BMDC membranes were extracted by incubating in RIPA buffer compromising 1 % volume of PIC for 30 min on ice. Protein concentrations were examined using the BCA method, followed by the separation of proteins on a 10 % SDS polyacrylamide gel. Subsequently, the running gels were stained using Coomassie Brilliant Blue R-250 solution. After destaining step, protein bands in SDS polyacrylamide gels were observed by a ChemiDoc Imaging System (Bio-Rad).

### 4.12. Evaluating the Si9GM uptake of BMDCs using bio-TEM

BMDCs were seeded on a 6-well plate at a density of $1 \times 10^6$ cells $mL^{-1}$ and incubated with Si9GM (50 μg $mL^{-1}$) for 12 h. Next, BMDCs were harvested and fixed with fixation buffer comprising a mixture of paraformaldehyde and glutaraldehyde (v/v = 2 %/2 %) in 0.05 M sodium cacodylate buffer (pH 7.2) at 4 °C for 4 h. Afterward, BMDCs were rinsed and re-fixed using 1 % osmium tetroxide in 0.1 M sodium cacodylate buffer (pH 7.2) at 4 °C for 2 h. After dehydration, treated BMDCs were embedded in resin and cured at 65 °C overnight for polymerization. The embedded specimens were cut into sections with a thickness of 100 nm. Finally, the slice was stained with 2.5 % uranyl acetate for 7 min followed by 2.5 % lead citrate for 2 min before being observed at 80 kV using a JEM 1011.

### 4.13. Evaluating the ability to escape lysosomal compartments of Si9GM

cDC1s were seeded on an 8-well Ibidi μ-Slide (Ibidi GmbH) at a cell density of $5 \times 10^4$ cells per well and then incubated with Si9GM (50 μg $mL^{-1}$) and 2′3′-cGAMP (1 μM). To monitor the colocation of nanovaccines and lysosomes at 8 h post-treatment, cDC1s were incubated with LysoTracker Red (50 nM) at 37 °C for 30 min. After that, cDC1s were rinsed twice with PBS and then subjected to nuclear staining with Hoechst 33342 (1 μg $mL^{-1}$) at 37 °C for 20 min. The cells were immediately imaged with a CLSM and fluorescence (LysoTracker Red, Ex/Em = 577 nm/590 nm; Hoechst 33342, Ex/Em = 350 nm/461 nm).

### 4.14. Evaluating the targeting ability of Si9GM in cDC1s

For CLEC9A receptor blocking, cDC1 cells at day 11 post-stimulation ($1 \times 10^6$ cells $mL^{-1}$) were incubated with TruStain FcX™ (anti-mouse CD16/32, 1 μg $mL^{-1}$) antibody for 15 min on ice to prevent the non-specific bindings of immunoglobulin to Fc receptors. Subsequently,

cDC1 cells were stained with purified αCLEC9A antibody (anti-mouse CLEC9A, BioXcell) at a αCLEC9A concentration of 0.3 μg $mL^{-1}$ of cDC1, and then incubated for 30 min on ice. The excess amount of antibody was removed by centrifugation. At this stage, as-prepared cDC1s can be used for the treatment. For the verification of the comprehensive blocking of CLEC9A receptors, the as-prepared cDC1s were stained by APC-labeled CLEC9A antibody (0.3 μg $mL^{-1}$) for 30 min on ice. After washing, cDC1s were analyzed by flow cytometry to determine the blocking efficacy.

After washing, αCLEC9A-blocking cDC1 cells and non-blocking cDC1 cells were seeded in 96-well plate at a cell density of $1 \times 10^5$ cells per well. After 2 h-incubation, cDC1 cells were treated by fluorescent-labeled Si9GM and fluorescent-labeled SiGM for the next 2 h. After that, cells were harvested and washed twice to eliminate the non-uptake nanoparticles. The percentage of uptake in αCLEC9A-blocking cDC1 cells and non-blocking cDC1 cells was analyzed by flow cytometry.

### 4.15. $CD8^+$ T cells isolation from mice spleens

Female C57BL/6 mice (7-week old), received subcutaneous injections of DC-$OVA_{257\text{-}264}$ three times at intervals of 3 days. One day post the last vaccination, the spleen was collected and cut into small pieces. After digestion into single cells, $CD8^+$ T cells were isolated by Mojosort isolation kit (BioLegend). In brief, cell density was adjusted into a concentration of $1 \times 10^6$ cells $mL^{-1}$ in MojoSort buffer and divided into 100 μL of cell suspension. Next, the biotin-antibody cocktail (10 μL) was added into each tube and incubated at 4 °C for 15 min. Subsequently, streptavidin nanobeads was vortexed and added into the above cell suspension, followed by the incubation on ice for 15 min. After that, MojoSort buffer (2.5 mL) was added. The stained splenic cells were then placed in the magnet for at least 5 min and the $CD8^+$ T cells were then carefully aliquoted into a new tube for subsequent experiments.

### 4.16. Observation of $CD8^+$ T cell interaction with Si9GM by CLSM

Splenic $CD8^+$ T cells were seeded on an 8-well Ibidi μ-Slide (Ibidi GmbH) at a cell density of $1 \times 10^5$ cells per well and incubated at 37 °C for 24 h. $CD8^+$ T cells were treated with Si9GM (50 μg $mL^{-1}$) at 37 °C for 30 min and rinsed by DPBS to remove the excess Si9GM NPs. After fixation at RT for 20 min, the T cells were stained by neuro-DiO at 37 °C for 30 min and Hoechst 33342 at 37 °C for 20 min, followed by CLSM observation.

### 4.17. Evaluation the ability of Si9GM in CD8 T cell activation and proliferation

$CD8^+$ T cells were isolated from spleens and LNs of OT-I mice (12-week-old, male/female). Spleens and LNs were then minced into single cell suspension in 10 % FBS-supplemented RPMI media containing collagenase IV (1 mg $mL^{-1}$) and DNase I (100 μg $mL^{-1}$). After washing, the number of cells was counted and $CD8^+$ T cells were isolated from the cell suspension using a CD8 T cell Mojosort isolation kit (BioLegend).

In an experiment to evaluate $CD8^+$ T cell activation, isolated $CD8^+$ T cells were seeded on 96-well plate at a cell density of $1 \times 10^5$ cells per well in 1 % FBS-supplemented RPMI media. Subsequently, $CD8^+$ T cells were treated by DC-OVA (1 mg $mL^{-1}$), Si9GimM (immature BMDC membrane coating, 100 μg $mL^{-1}$), Si9GM (100 μg $mL^{-1}$), and CD3/CD24 Dynabeads ($2 \times 10^5$ beads per well) for 20 h. After that, $CD8^+$ T cells were harvested and stained by CD69 antibody for flow cytometric analysis.

In an experiment to evaluate $CD8^+$ T cell proliferation, isolated $CD8^+$ T cells were stained by CSFE (5 μM) in 10 mM PBS pH 7.4 for 20 min at 37 °C at a cell density of $1 \times 10^7$ cells per mL. After washing to remove the excess CFSE, $CD8^+$ T cells were seeded on 96-well plate at a cell density of $1 \times 10^5$ cells per well in 10 % FBS-supplemented RPMI media. After 15 min of incubation, $CD8^+$ T cells were treated by DC-OVA (1 mg $mL^{-1}$), Si9GimM (immature BMDC membrane coating, 100 μg $mL^{-1}$), Si9GM (100 μg $mL^{-1}$), and CD3/CD24 Dynabeads ($2 \times 10^5$ beads per well, in addition of IL-2 _ 50 IU $mL^{-1}$). The plate was incubated at 37 °C for 4 days. A half media in each well were replaced by the fresh 10 % FBS-supplemented RPMI media every 48 h. At day 4, $CD8^+$ T cells were harvested for flow cytometric analysis.

### 4.18. Evaluation the killing efficacy of cytotoxic $CD8^+$ T cells to B16-OVA cancer cells

B16-OVA cancer cells were seeded on 24-well plate at a cell density of $1 \times 10^5$ cells per well in 10 % FBS-supplemented RPMI media, incubated overnight at 37 °C. Otherwise, cytotoxic $CD8^+$ T cells at day 4 in the T cell proliferation experiment were added to B16-OVA cells (B16-OVA: CD8 T = 1 : 4) and incubated for 20 h at 37 °C. Subsequently, all cells were harvested and stained by CD3 antibody and then live/dead staining kit (PI/Annexin V- FITC) for flow cytometric analysis.

### 4.19. Characterization of DC maturation

BMDCs were seeded on tissue culture (TC)-treated 6-well plates at a cell density of $1 \times 10^6$ cells $mL^{-1}$ and then incubated in 1 % HI-FBS RPMI-1640 containing 2′3′-cGAMP (10 μM) or Si9GM (100 μg $mL^{-1}$) for 24 h. Once cells were harvested, BMDCs were stained with antibodies specific for mature DCs: FITC anti-mouse CD11c, Alexa 700 anti-mouse MHC II, Alexa 647 anti-mouse CD40, PE dazzle 594 anti-mouse CCR7, and PE/Dazzle™ 594 anti-mouse H-2K $^b$ bound to SIINFEKL. The incubation was carried out for 30 min on ice. After that, the characterization of DC maturation was performed using a FACSAria™ Fusion (BD Biosciences). Data were analyzed with FlowJo software (version 10.8.1).

### 4.20. Biodistribution and lymph node imaging

cFAET-labeled 2′3′-cGAMP and cFAET-labeled 2′3′- cGAMP@Si9GM (6 μg of cFAET-labeled 2′3′-cGAMP per mouse) were subcutaneously injected into of C57BL/6 mice. Subsequently, the kinetic fluorescence distributions of cFAET-labeled 2′3′-cGAMP were examined at 0, 2, 4, 8, 12, 24, and 48 h postinjection with an in vivo imaging system (FOBI in vivo imaging system, NeoScience). To verify the distribution of nanovaccines, inguinal lymph nodes and key organs (heart, liver, spleen, lung, and kidney) were extracted for ex vivo fluorescence imaging 12 h following vaccination. For verification of the interaction between T cells and nanovaccines in vivo, DiR-labeled Si9GM (200 μg of DHPSi-$NH_2$ per mouse) was subcutaneously injected, and LNs were collected for high-magnification confocal examination. The lymph nodes were cut into sections (10 μm-thick) and incubated with anti-CD3 antibody (Biolegend catalog no. 100340, diluted 1:50) overnight at 4 °C. They were then treated with Goat anti-hamster IgG antibody (Biolegend catalog no. 405508, diluted 1:100) for 1 h at RT. Following washing with PBS-Tween, the tissue sections underwent DAPI staining for 5 min at room temperature before being washed again with PBS-Tween. The tissue sections were imaged using a confocal laser scanning microscope.

### 4.21. In vivo maturation of cDC1s and $CD8^+$ T-cell priming

C57BL/6 mice (7-week-old, female, n = 3 for each group) were shaved and then subcutaneously injected with B16-OVA cells ($2.5 \times 10^6$ cells per mouse). Ten days after inoculation, mice were vaccinated three times at intervals of 3 days (50 μg free 2′3′-cGAMP, and NVs dose comprising 5 μg of 2′3′-cGAMP per mouse). On day 8, and day 10 post the first vaccination, mice spleens and tumors were harvested for immune cell analysis, respectively. Briefly, spleens and tumors were digested in a solution comprising collagenase type IV (1 mg $mL^{-1}$) and DNase I (100 μg $mL^{-1}$) to obtain single cells. Subsequently, cell suspensions were treated with RBC lysis buffer to eliminate red blood cells, followed by blocking Fc receptors. Next, cell suspensions were stained

by specific antibodies for flow cytometry analysis. Flow cytometric analyses were performed using a BD FACSAria Fusion. FlowJo software (version 10.8.1) was used to analyze data.

### 4.22. In vivo immune responses

C57BL/6 mice (7-week-old, female, n = 5 for each group) were shaved and then subcutaneously injected with B16-OVA cells ($1.5 \times 10^5$ cells per mouse). Seven days after inoculation (50 μg free 2′3′-cGAMP, and NVs dose comprising 5 μg of 2′3′-cGAMP per mouse), mice were vaccinated 4 times at intervals of 3 days. Subsequently, LNs, spleens, and tumors were collected on the assigned day and further digested into cell suspension by collagenase type IV (1 mg $mL^{-1}$) and DNase I (100 μg $mL^{-1}$). The cell suspension was centrifuged at 350 g for 5 min; the collected cells were resuspended with RBC lysis buffer at 4 °C for 5 min to lysis red blood cells. The lysis was terminated by 10 % FBS RPMI. Single cells were obtained by filtration through a cell strainer (70 μm pore-size) and washed with FACS staining buffer for immune cell staining according to the protocol for surface proteins, intracellular proteins, and nuclear protein staining. Flow cytometric analyses were performed using a BD FACSAria Fusion. FlowJo software (version 10.8.1) was used to analyze flow cytometric data.

### 4.23. In vivo anti-metastasis capability

C57BL/6 mice (6-week-old, female, n = 5 for each group) were injected intravenously with B16-OVA melanoma cells ($1.5 \times 10^5$ per mouse). Mice were immunized by subcutaneous injection (50 μg free 2′3′-cGAMP, and NVs dose comprising 5 μg of 2′3′-cGAMP per mouse) at the right leg (a total of 4 vaccinations with 3-day intervals). All mice were euthanized on day 20, and lungs were harvested and weighed. All lung tissues were used for H & E staining and FACS analysis. Lungs were sectioned into small fragments of 1–2 mm in length and then digested in 10 % RPMI-1640 supplemented with collagenase type IV (1 mg $mL^{-1}$) and DNase I (100 μg $mL^{-1}$) at 37 °C for 20 min, followed by filtration through a 70 μm cell strainer. After that, single cells were treated with RBC lysis buffer for 3 min at RT. The isolated cells were washed with cell staining buffer and stained as in the manufacturer's protocol. Flow cytometry analyses were carried out using a BD FACS Aria Fusion. Data were analyzed with FlowJo software (version 10.8.1).

### 4.24. In vivo immune cell depletion for lung anti-metastasis evaluation

C57BL/6 mice (7-week-old, female, n = 5 for each group) were injected intravenously with B16-OVA melanoma cells ($1.5 \times 10^5$ cells per mouse) and divided into four groups (G1, G2, G3, G4). After 1 day, each group was subjected to an antibody through intraperitoneal injection. For NK cell depletion (G3), mice were i.p. injected with anti-NK 1.1 antibody (200 μg per mouse) at day −1, day 2, and day 5. For CD8 T cell depletion (G4), mice were i.p. injected with anti-CD8α antibody (200 μg per mouse) at day −1 and then at that same dosage at day 2 and day 5. For a control group (G2), mouse IgG2a antibody (200 μg per mouse) was i.p. injected at the same schedule as G3 and G4. Si9GM (NVs dose comprising 5 μg of 2′3′-cGAMP per mouse) was injected into mice of G3 and G4 at days 0, 3, and 6. On day 20, all lung tissues were collected, weighed, and used for H & E staining and flow cytometric analysis as mentioned above. Flow cytometric analyses were performed using a BD FACSAria Fusion. Data were analyzed with FlowJo software (version 10.8.1).

### 4.25. Statistical analysis

All experiments were carried out in triplicates unless otherwise mentioned specifically. The data are presented as mean ± standard deviation (S.D.) of the mean. Statistical significance was evaluated using one-way or two-way analysis of variance (ANOVA) and T-test with the Graph-Pad Prism 8 software (version 10.8.1). Survival was illustrated using the Kaplan–Meier method. A P-value <0.05 was considered statistically significant (*P < 0.05; **P < 0.01; ***P < 0.001; ****P < 0.0001); ns: no significant difference.

## Ethics approval and consent to participate

Animal care strictly followed the law issued by the National Institute of Health (NIH publication 80-23, revised in 1996). All animal experiments were conducted following thorough review and approval by the Institutional Animal Care and Use Committee (IACUC) of Sungkyunkwan University (IACUC number: 202310631).

## CRediT authorship contribution statement

**Nguyen Thi Nguyen:** Writing – review & editing, Writing – original draft, Visualization, Validation, Methodology, Investigation, Formal analysis, Data curation, Conceptualization. **Xuan Thien Le:** Validation, Methodology, Investigation, Formal analysis. **Woo Tak Lee:** Validation, Data curation. **Yong Taik Lim:** Data curation. **Kyung Taek Oh:** Writing – review & editing. **Eun Seong Lee:** Writing – review & editing. **Han-Gon Choi:** Writing – review & editing. **Yu Seok Youn:** Writing – review & editing, Supervision, Project administration, Funding acquisition, Data curation, Conceptualization.

## Declaration of competing interest

All authors declare no competing financial interest.

## Acknowledgments

This work was supported by a National Research Foundation of Korea (NRF) grant funded by the Korean government (MSIT; No. RS-2024-00352440 and No. NRF-2019R1A5A2027340). We thank Prof. Yong Taik Lim for providing OT-I mice from Laboratory for Immune Modulation, Sungkyunkwan University. Some parts of the schematic illustrations in Graphical abstract, Scheme 1, Figs. 1A–4A and 5A–Fig. 6A, Fig. 6B–Fig. 7A, and Fig. 8A were created with BioRender.com.

## Appendix A. Supplementary data

Supplementary data to this article can be found online at https://doi.org/10.1016/j.bioactmat.2024.09.002.

## References

[1] A.R. Shokouhi, Y. Chen, H.Z. Yoh, J. Brenker, T. Alan, T. Murayama, K. Suu, Y. Morikawa, N.H. Voelcker, R. Elnathan, Engineering efficient CAR-T cells via electroactive nanoinjection, Adv. Mater. 35 (44) (2023) e2304122, https://doi.org/10.1002/adma.202304122.

[2] R. Grosser, L. Cherkassky, N. Chintala, P.S. Adusumilli, Combination immunotherapy with CAR T cells and checkpoint blockade for the treatment of solid tumors, Cancer Cell 36 (5) (2019) 471–482, https://doi.org/10.1016/j.ccell.2019.09.006.

[3] Y. Jiang, N. Krishnan, J. Zhou, S. Chekuri, X. Wei, A.V. Kroll, C.L. Yu, Y. Duan, W. Gao, R.H. Fang, L. Zhang, Engineered cell-membrane-coated nanoparticles directly present tumor antigens to promote anticancer immunity, Adv. Mater. 32 (30) (2020) e2001808, https://doi.org/10.1002/adma.202001808.

[4] S. Go, M. Jung, S. Lee, S. Moon, J. Hong, C. Kim, Y.S. Chung, B.S. Kim, A personalized cancer nanovaccine that enhances T-cell responses and efficacy through dual interactions with dendritic cells and T cells, Adv. Mater. 35 (49) (2023), https://doi.org/10.1002/adma.202303979.

[5] S. Yu, C. Wang, J. Yu, J. Wang, Y. Lu, Y. Zhang, X. Zhang, Q. Hu, W. Sun, C. He, X. Chen, Z. Gu, Injectable bioresponsive gel depot for enhanced immune checkpoint blockade, Adv. Mater. 30 (28) (2018) e1801527, https://doi.org/10.1002/adma.201801527.

[6] C. Wang, W.J. Sun, Y.Q. Ye, Q.Y. Hu, H.N. Bomba, Z. Gu, Activation of platelets with checkpoint inhibitors for post-surgical cancer immunotherapy, Nat. Biomed. Eng. 1 (2) (2017), https://doi.org/10.1038/s41551-016-0011.

[7] J.Y. Ye, B. Hou, M. Saeed, Z.A. Xu, H.J. Yu, Engineering bioinspired nanomedicines to mitigate the resistance to cancer immunotherapy, Acc. Mater. Res. (2022), https://doi.org/10.1021/accountsmr.2c00042.
[8] Y. Zeng, S. Li, S. Zhang, L. Wang, H. Yuan, F. Hu, Cell membrane coated-nanoparticles for cancer immunotherapy, Acta Pharm. Sin. B 12 (8) (2022) 3233–3254, https://doi.org/10.1016/j.apsb.2022.02.023.
[9] Y. Huang, X. Gao, J. Chen, Leukocyte-derived biomimetic nanoparticulate drug delivery systems for cancer therapy, Acta Pharm. Sin. B 8 (1) (2018) 4–13, https://doi.org/10.1016/j.apsb.2017.12.001.
[10] R.H. Fang, Y. Jiang, J.C. Fang, L. Zhang, Cell membrane-derived nanomaterials for biomedical applications, Biomaterials 128 (2017) 69–83, https://doi.org/10.1016/j.biomaterials.2017.02.041.
[11] N.T. Nguyen, J. Kim, X.T. Le, W.T. Lee, E.S. Lee, K.T. Oh, H.G. Choi, Y.S. Youn, Amplified fenton-based oxidative stress utilizing ultraviolet upconversion luminescence-fueled nanoreactors for apoptosis-strengthened ferroptosis anticancer therapy, ACS Nano 17 (1) (2023) 382–401, https://doi.org/10.1021/acsnano.2c08706.
[12] J. Constantino, C. Gomes, A. Falcao, B.M. Neves, M.T. Cruz, Dendritic cell-based immunotherapy: a basic review and recent advances, Immunol. Res. 65 (4) (2017) 798–810, https://doi.org/10.1007/s12026-017-8931-1.
[13] F. Oroojalian, M. Beygi, B. Baradaran, A. Mokhtarzadeh, M.A. Shahbazi, Immune cell membrane-coated biomimetic nanoparticles for targeted cancer therapy, Small 17 (12) (2021) e2006484, https://doi.org/10.1002/smll.202006484.
[14] J.A. Soto, N.M.S. Galvez, C.A. Andrade, G.A. Pacheco, K. Bohmwald, R.V. Berrios, S.M. Bueno, A.M. Kalergis, The role of dendritic cells during infections caused by highly prevalent viruses, Front. Immunol. 11 (2020) 1513, https://doi.org/10.3389/fimmu.2020.01513.
[15] T.R. Mempel, S.E. Henrickson, U.H. Von Andrian, T-cell priming by dendritic cells in lymph nodes occurs in three distinct phases, Nature 427 (6970) (2004) 154–159, https://doi.org/10.1038/nature02238.
[16] A.M. Dudek, S. Martin, A.D. Garg, P. Agostinis, Immature, semi-mature, and fully mature dendritic cells: toward a DC-cancer cells interface that augments anticancer immunity, Front. Immunol. 4 (2013) 438, https://doi.org/10.3389/fimmu.2013.00438.
[17] C. Liu, X. Liu, X.C. Xiang, X. Pang, S.Y. Chen, Y.M. Zhang, E. Ren, L.L. Zhang, X. Liu, P. Lv, X.Y. Wang, W.X. Luo, N.S. Xia, X.Y. Chen, G. Liu, A nanovaccine for antigen self-presentation and immunosuppression reversal as a personalized cancer immunotherapy strategy, Nat. Nanotechnol. 17 (5) (2022) 531–540, https://doi.org/10.1038/s41565-022-01098-0.
[18] M. Jung, M. Kang, B.S. Kim, J. Hong, C. Kim, C.H. Koh, G. Choi, Y. Chung, B.S. Kim, Nanovesicle-mediated targeted delivery of immune checkpoint blockades to potentiate therapeutic efficacy and prevent side effects, Adv. Mater. 34 (9) (2022) e2106516, https://doi.org/10.1002/adma.202106516.
[19] S. Cheng, C. Xu, Y. Jin, Y. Li, C. Zhong, J. Ma, J. Yang, N. Zhang, Y. Li, C. Wang, Z. Yang, Y. Wang, Artificial mini dendritic cells boost T cell-based immunotherapy for ovarian cancer, Adv. Sci. 7 (7) (2020) 1903301, https://doi.org/10.1002/advs.201903301.
[20] X.Y. Ma, L. Kuang, Y. Yin, L. Tang, Y. Zhang, Q. Fan, B.Y. Wang, Z.F. Dong, W. Wang, T.Y. Yin, Y.Z. Wang, Tumor-antigen activated dendritic cell membrane-coated biomimetic nanoparticles with orchestrating immune responses promote therapeutic efficacy against glioma, ACS Nano 17 (3) (2023) 2341–2355, https://doi.org/10.1021/acsnano.2c09033.
[21] J. Zhang, B. Fan, G.L. Cao, W.P. Huang, F.H. Jia, G.J. Nie, H. Wang, Direct presentation of tumor-associated antigens to induce adaptive immunity by personalized dendritic cell-mimicking nanovaccines, Adv. Mater. 34 (47) (2022), https://doi.org/10.1002/adma.202205950.
[22] J.A. Hubbell, M.A. Swartz, Trojan horses for immunotherapy, Nat. Nanotechnol. 14 (3) (2019) 196–197, https://doi.org/10.1038/s41565-019-0380-7.
[23] V.K. Gonugunta, T. Sakai, V. Pokatayev, K. Yang, J. Wu, N. Dobbs, N. Yan, Trafficking-mediated sting degradation requires sorting to acidified endolysosomes and can be targeted to enhance anti-tumor response, Cell Rep. 21 (11) (2017) 3234–3242, https://doi.org/10.1016/j.celrep.2017.11.061.
[24] F. Chen, T. Li, H. Zhang, M. Saeed, X. Liu, L. Huang, X. Wang, J. Gao, B. Hou, Y. Lai, C. Ding, Z. Xu, Z. Xie, M. Luo, H. Yu, Acid-ionizable iron nanoadjuvant augments sting activation for personalized vaccination immunotherapy of cancer, Adv. Mater. 35 (10) (2023) e2209910, https://doi.org/10.1002/adma.202209910.
[25] L. Wang, H. Zhou, Q. Chen, Z. Lin, C. Jiang, X. Chen, M. Chen, L. Liu, L. Shao, X. Liu, J. Pan, J. Wu, J. Song, J. Wu, D. Zhang, STING agonist-loaded nanoparticles promotes positive regulation of type I interferon-dependent radioimmunotherapy in rectal cancer, Adv. Sci. 11 (7) (2024) e2307858, https://doi.org/10.1002/advs.202307858.
[26] M. Luo, H. Wang, Z. Wang, H. Cai, Z. Lu, Y. Li, M. Du, G. Huang, C. Wang, X. Chen, M.R. Porembka, J. Lea, A.E. Frankel, Y.X. Fu, Z.J. Chen, J. Gao, A STING-activating nanovaccine for cancer immunotherapy, Nat. Nanotechnol. 12 (7) (2017) 648–654, https://doi.org/10.1038/nnano.2017.52.
[27] D.D. Xu, J. Hu, J.W. Mei, J. Zhou, Z.X. Wang, X.D. Zhang, Q. Liu, Z. Su, W.B. Zhu, H.J. Liu, C. Zhu, Nanoadjuvant-triggered STING activation evokes systemic immunotherapy for repetitive implant-related infections, Bioact. Mater. 35 (2024) 82–98, https://doi.org/10.1016/j.bioactmat.2024.01.020.
[28] H. Zheng, B.B. Guo, X.Y. Qiu, Y.F. Xia, Y. Qu, L. Cheng, F.H. Meng, Z.Y. Zhong, Polymersome-mediated cytosolic delivery of cyclic dinucleotide sting agonist enhances tumor immunotherapy, Bioact. Mater. 16 (2022) 1–11, https://doi.org/10.1016/j.bioactmat.2022.02.029.
[29] Y. Li, X. Li, J. Yi, Y. Cao, Z. Qin, Z. Zhong, W. Yang, Nanoparticle-mediated sting activation for cancer immunotherapy, Adv. Healthcare Mater. 12 (19) (2023) e2300260, https://doi.org/10.1002/adhm.202300260.
[30] D. Shae, K.W. Becker, P. Christov, D.S. Yun, A.K.R. Lytton-Jean, S. Sevimli, M. Ascano, M. Kelley, D.B. Johnson, J.M. Balko, J.T. Wilson, Endosomolytic polymersomes increase the activity of cyclic dinucleotide sting agonists to enhance cancer immunotherapy, Nat. Nanotechnol. 14 (3) (2019) 269–278, https://doi.org/10.1038/s41565-018-0342-5.
[31] X. Sun, Y. Zhang, J. Li, K.S. Park, K. Han, X. Zhou, Y. Xu, J. Nam, J. Xu, X. Shi, L. Wei, Y.L. Lei, J.J. Moon, Amplifying sting activation by cyclic dinucleotide-manganese particles for local and systemic cancer metalloimmunotherapy, Nat. Nanotechnol. 16 (11) (2021) 1260–1270, https://doi.org/10.1038/s41565-021-00962-9.
[32] P. Dosta, A.M. Cryer, M.Z. Dion, T. Shiraishi, S.P. Langston, D. Lok, J. Wang, S. Harrison, T. Hatten, M.L. Ganno, V.A. Appleman, G.M. Taboada, N. Puigmal, S. Ferber, S. Kalash, M. Prado, A.L. Rodriguez, W.S. Kamoun, A.O. Abu-Yousif, N. Artzi, Investigation of the enhanced antitumour potency of STING agonist after conjugation to polymer nanoparticles, Nat. Nanotechnol. 18 (11) (2023) 1351–1363, https://doi.org/10.1038/s41565-023-01447-7.
[33] J.P. Bottcher, C. Reis e Sousa, The role of type 1 conventional dendritic cells in cancer immunity, Trends Cancer 4 (11) (2018) 784–792, https://doi.org/10.1016/j.trecan.2018.09.001.
[34] X. Ma, L. Kuang, Y. Yin, L. Tang, Y. Zhang, Q. Fan, B. Wang, Z. Dong, W. Wang, T. Yin, Y. Wang, Tumor-antigen activated dendritic cell membrane-coated biomimetic nanoparticles with orchestrating immune responses promote therapeutic efficacy against glioma, ACS Nano 17 (3) (2023) 2341–2355, https://doi.org/10.1021/acsnano.2c09033.
[35] G. Schreibelt, L.J. Klinkenberg, L.J. Cruz, P.J. Tacken, J. Tel, M. Kreutz, G. J. Adema, G.D. Brown, C.G. Figdor, I.J. de Vries, The C-type lectin receptor CLEC9A mediates antigen uptake and (cross-)presentation by human blood BDCA3 + myeloid dendritic cells, Blood 119 (10) (2012) 2284–2292, https://doi.org/10.1182/blood-2011-08-373944.
[36] D. Sancho, O.P. Joffre, A.M. Keller, N.C. Rogers, D. Martínez, P. Hernanz-Falcón, I. Rosewell, C.R.E. Sousa, Identification of a dendritic cell receptor that couples sensing of necrosis to immunity, Nature 458 (7240) (2009) 899–903, https://doi.org/10.1038/nature07750.
[37] Y. Kato, T.M. Steiner, H.Y. Park, R.O. Hitchcock, A. Zaid, J.L. Hor, S. Devi, G. M. Davey, D. Vremec, K.M. Tullett, P.S. Tan, F. Ahmet, S.N. Mueller, S. Alonso, D. M. Tarlinton, H.L. Ploegh, T. Kaisho, L. Beattie, J.H. Manton, D. Fernandez-Ruiz, K. Shortman, M.H. Lahoud, W.R. Heath, I. Caminschi, Display of native antigen on cDC1 that have spatial access to both T and B cells underlies efficient humoral vaccination, J. Immunol. 205 (7) (2020) 1842–1856, https://doi.org/10.4049/jimmunol.2000549.
[38] M. Sela, M. Poley, P. Mora-Raimundo, S. Kagan, A. Avital, M. Kaduri, G. Chen, O. Adir, A. Rozencweig, Y. Weiss, O. Sade, Y. Leichtmann-Bardoogo, L. Simchi, S. Aga-Mizrachi, B. Bell, Y. Yeretz-Peretz, A.Z. Or, A. Choudhary, I. Rosh, D. Cordeiro, S. Cohen-Adiv, Y. Berdichevsky, A. Odeh, J. Shklover, J. Shainsky-Roitman, J.E. Schroeder, D. Hershkovitz, P. Hasson, A. Ashkenazi, S. Stern, T. Laviv, A. Ben-Zvi, A. Avital, U. Ashery, B.M. Maoz, A. Schroeder, Brain-targeted liposomes loaded with monoclonal antibodies reduce alpha-synuclein aggregation and improve behavioral symptoms in Parkinson's disease, Adv. Mater. 35 (51) (2023) e2304654, https://doi.org/10.1002/adma.202304654.
[39] X. Xie, Y. Hu, T. Ye, Y. Chen, L. Zhou, F. Li, X. Xi, S. Wang, Y. He, X. Gao, W. Wei, G. Ma, Y. Li, Therapeutic vaccination against leukaemia via the sustained release of co-encapsulated anti-PD-1 and a leukaemia-associated antigen, Nat. Biomed. Eng. 5 (5) (2021) 414–428, https://doi.org/10.1038/s41551-020-00624-6.
[40] G. Jiang, Z. Huang, Y. Yuan, K. Tao, W. Feng, Intracellular delivery of anti-BCR/ABL antibody by PLGA nanoparticles suppresses the oncogenesis of chronic myeloid leukemia cells, J. Hematol. Oncol. 14 (1) (2021) 139, https://doi.org/10.1186/s13045-021-01150-x.
[41] X. Du, B. Shi, J. Liang, J. Bi, S. Dai, S.Z. Qiao, Developing functionalized dendrimer-like silica nanoparticles with hierarchical pores as advanced delivery nanocarriers, Adv. Mater. 25 (41) (2013) 5981–5985, https://doi.org/10.1002/adma.201302189.
[42] N.K. Campbell, H.K. Fitzgerald, A. Malara, R. Hambly, C.M. Sweeney, B. Kirby, J. M. Fletcher, A. Dunne, Naturally derived heme-oxygenase 1 inducers attenuate inflammatory responses in human dendritic cells and T cells: relevance for psoriasis treatment, Sci. Rep. 8 (1) (2018) 10287, https://doi.org/10.1038/s41598-018-28488-6.
[43] C. Admyre, S.M. Johansson, S. Paulie, S. Gabrielsson, Direct exosome stimulation of peripheral human T cells detected by elispot, Eur. J. Immunol. 36 (7) (2006) 1772–1781, https://doi.org/10.1002/eji.200535615.
[44] S.M. Jin, Y.J. Yoo, H.S. Shin, S. Kim, S.N. Lee, C.H. Lee, H. Kim, J.E. Kim, Y.S. Bae, J. Hong, Y.W. Noh, Y.T. Lim, A nanoadjuvant that dynamically coordinates innate immune stimuli activation enhances cancer immunotherapy and reduces immune cell exhaustion, Nat. Nanotechnol. 18 (4) (2023), https://doi.org/10.1038/s41565-022-01296-w.
[45] T. Su, Y. Zhang, K. Valerie, X.Y. Wang, S. Lin, G. Zhu, STING activation in cancer immunotherapy, Theranostics 9 (25) (2019) 7759–7771, https://doi.org/10.7150/thno.37574.
[46] M.P. Longhi, C. Trumpfheller, J. Idoyaga, M. Caskey, I. Matos, C. Kluger, A. M. Salazar, M. Colonna, R.M. Steinman, Dendritic cells require a systemic type I interferon response to mature and induce CD4+ Th1 immunity with poly IC as adjuvant, J. Exp. Med. 206 (7) (2009) 1589–1602, https://doi.org/10.1084/jem.20090247.
[47] J. Guo, L. Huang, Nanodelivery of cGAS-STING activators for tumor immunotherapy, Trends Pharmacol. Sci. 43 (11) (2022) 957–972, https://doi.org/10.1016/j.tips.2022.08.006.

[48] M.F. Gulen, U. Koch, S.M. Haag, F. Schuler, L. Apetoh, A. Villunger, F. Radtke, A. Ablasser, Signalling strength determines proapoptotic functions of STING, Nat. Commun. 8 (2017), https://doi.org/10.1038/s41467-017-00573-w.
[49] J.W. Hickey, F.P. Vicente, G.P. Howard, H.Q. Mao, J.P. Schneck, Biologically inspired design of nanoparticle artificial antigen-presenting cells for immunomodulation, Nano Lett. 17 (11) (2017) 7045–7054, https://doi.org/10.1021/acs.nanolett.7b03734.
[50] O. Danilchanka, J.J. Mekalanos, Cyclic dinucleotides and the innate immune response, Cell 154 (5) (2013) 962–970, https://doi.org/10.1016/j.cell.2013.08.014.
[51] A. Decout, J.D. Katz, S. Venkatraman, A. Ablasser, The cGAS-STING pathway as a therapeutic target in inflammatory diseases, Nat. Rev. Immunol. 21 (9) (2021) 548–569, https://doi.org/10.1038/s41577-021-00524-z.
[52] A. Basit, M.G. Cho, E.Y. Kim, D. Kwon, S.J. Kang, J.H. Lee, The cGAS/STING/TBK1/IRF3 innate immunity pathway maintains chromosomal stability through regulation of p21 levels, Exp. Mol. Med. 52 (4) (2020) 643–657, https://doi.org/10.1038/s12276-020-0416-y.
[53] R. Fang, Q. Jiang, X. Zhou, C. Wang, Y. Guan, J. Tao, J. Xi, J.M. Feng, Z. Jiang, MAVS activates TBK1 and IKKε through TRAFs in nemo dependent and independent manner, PLoS Pathog. 13 (11) (2017) e1006720, https://doi.org/10.1371/journal.ppat.1006720.
[54] G. Schuler, R.M. Steinman, Murine epidermal langerhans cells mature into potent immunostimulatory dendritic cells in vitro, J. Exp. Med. 161 (3) (1985) 526–546, https://doi.org/10.1084/jem.161.3.526.
[55] J. Liu, X. Zhang, Y. Cheng, X. Cao, Dendritic cell migration in inflammation and immunity, Cell. Mol. Immunol. 18 (11) (2021) 2461–2471, https://doi.org/10.1038/s41423-021-00726-4.
[56] M. Buettner, U. Bode, Lymph node dissection - understanding the immunological function of lymph nodes, Clin. Exp. Immunol. 169 (3) (2012) 205–212, https://doi.org/10.1111/j.1365-2249.2012.04602.x.
[57] A. He, X. Li, Z. Dai, Q. Li, Y. Zhang, M. Ding, Z.F. Wen, Y. Mou, H. Dong, Nanovaccine-based strategies for lymph node targeted delivery and imaging in tumor immunotherapy, J. Nanobiotechnol. 21 (1) (2023) 236, https://doi.org/10.1186/s12951-023-01989-x.
[58] G. Ghislat, A.S. Cheema, E. Baudoin, C. Verthuy, P.J. Ballester, K. Crozat, N. Attaf, C. Dong, P. Milpied, B. Malissen, N. Auphan-Anezin, T.P.V. Manh, M. Dalod, T. Lawrence, NF- κB-dependent IRF1 activation programs cDC1 dendritic cells to drive antitumor immunity, Sci Immunol 6 (61) (2021), https://doi.org/10.1126/sciimmunol.abg3570.
[59] J. Wang, S. Li, M. Wang, X. Wang, S. Chen, Z. Sun, X. Ren, G. Huang, B.D. Sumer, N. Yan, Y.X. Fu, J. Gao, STING licensing of type I dendritic cells potentiates antitumor immunity, Sci Immunol 9 (92) (2024) eadj3945, https://doi.org/10.1126/sciimmunol.adj3945.
[60] K.E. Pauken, E.J. Wherry, Overcoming T cell exhaustion in infection and cancer, Trends Immunol. 36 (4) (2015) 265–276, https://doi.org/10.1016/j.it.2015.02.008.
[61] S. Chen, A. Saeed, Q. Liu, Q. Jiang, H. Xu, G.G. Xiao, L. Rao, Y. Duo, Macrophages in immunoregulation and therapeutics, Signal Transduct. Targeted Ther. 8 (1) (2023) 207, https://doi.org/10.1038/s41392-023-01452-1.
[62] L.S. Dungan, N.C. McGuinness, L. Boon, M.A. Lynch, K.H. Mills, Innate IFN-γ promotes development of experimental autoimmune encephalomyelitis: a role for NK cells and M1 macrophages, Eur. J. Immunol. 44 (10) (2014) 2903–2917, https://doi.org/10.1002/eji.201444612.
[63] S. Wang, J. Wang, Z. Chen, J. Luo, W. Guo, L. Sun, L. Lin, Targeting M2-like tumor-associated macrophages is a potential therapeutic approach to overcome antitumor drug resistance, npj Precis. Oncol. 8 (1) (2024) 31, https://doi.org/10.1038/s41698-024-00522-z.
[64] L. Hidalgo-Garcia, J. Galvez, M.E. Rodriguez-Cabezas, P.O. Anderson, Can a conversation between mesenchymal stromal cells and macrophages solve the crisis in the inflamed intestine? Front. Pharmacol. 9 (2018) 179, https://doi.org/10.3389/fphar.2018.00179.
[65] Y. Takeuchi, H. Nishikawa, Roles of regulatory T cells in cancer immunity, Int. Immunol. 28 (8) (2016) 401–409, https://doi.org/10.1093/intimm/dxw025.
[66] A. Marcus, A.J. Mao, M. Lensink-Vasan, L. Wang, R.E. Vance, D.H. Raulet, Tumor-derived cgamp triggers a STING-mediated interferon response in non-tumor cells to activate the NK cell response, Immunity 49 (4) (2018) 754–763, https://doi.org/10.1016/j.immuni.2018.09.016, e1-e4.
[67] X. Guan, Cancer metastases: challenges and opportunities, Acta Pharm. Sin. B 5 (5) (2015) 402–418, https://doi.org/10.1016/j.apsb.2015.07.005.
[68] M. Vyas, M. Requesens, T.H. Nguyen, D. Peigney, M. Azin, S. Demehri, Natural killer cells suppress cancer metastasis by eliminating circulating cancer cells, Front. Immunol. 13 (2022) 1098445, https://doi.org/10.3389/fimmu.2022.1098445.
[69] T. Nakamura, T. Sato, R. Endo, S. Sasaki, N. Takahashi, Y. Sato, M. Hyodo, Y. Hayakawa, H. Harashima, STING agonist loaded lipid nanoparticles overcome anti-PD-1 resistance in melanoma lung metastasis via NK cell activation, J Immunother Cancer 9 (7) (2021), https://doi.org/10.1136/jitc-2021-002852.
[70] X. Du, X. Li, H. Huang, J. He, X. Zhang, Dendrimer-like hybrid particles with tunable hierarchical pores, Nanoscale 7 (14) (2015) 6173–6184, https://doi.org/10.1039/c5nr00640f.
[71] S. Gou, W. Liu, S. Wang, G. Chen, Z. Chen, L. Qiu, X. Zhou, Y. Wu, Y. Qi, Y. Gao, Engineered nanovaccine targeting clec9a(+) dendritic cells remarkably enhances the cancer immunotherapy effects of sting agonist, Nano Lett. 21 (23) (2021) 9939–9950, https://doi.org/10.1021/acs.nanolett.1c03243.
[72] L. Liu, S. Fan, Z. Lu, Z. Chen, C. Chu, A. Liu, F. Xia, S. Meng, F. Guo, H. Qiu, Y. Yang, An optimized method for the induction and purification of mouse bone marrow dendritic cells, J. Immunol. Methods 495 (2021) 113073, https://doi.org/10.1016/j.jim.2021.113073.
[73] D. van Dinther, H. Veninga, M. Revet, L. Hoogterp, K. Olesek, J. Grabowska, E.G. F. Borg, H. Kalay, Y. van Kooyk, J.M.M. den Haan, Comparison of protein and peptide targeting for the development of a CD169-based vaccination strategy against melanoma, Front. Immunol. 9 (2018) 1997, https://doi.org/10.3389/fimmu.2018.01997.